

# Local-to-global signal transduction at the core of the $\text{Mn}^{2+}$ sensing riboswitch

Krishna C. Suddala<sup>1\*</sup>, Ian R. Price<sup>2\*</sup>, Michal Janeček<sup>3</sup>, Petra Kührová<sup>4</sup>, Shiba Dandpat<sup>1</sup>, Jiří Šponer<sup>3,4</sup>, Pavel Banáš<sup>3,4</sup>, Ailong Ke<sup>2</sup>, Nils G. Walter<sup>1</sup>

<sup>1</sup>Single Molecule Analysis Group and Center for RNA Biomedicine, Department of Chemistry, University of Michigan, Ann Arbor, MI, 48105,

<sup>2</sup>Department of Molecular Biology and Genetics, Cornell University, Ithaca, NY 14850

<sup>3</sup>Institute of Biophysics of the Czech Academy of Sciences, Kralovopolská 135, 612 65 Brno, Czech Republic

<sup>4</sup>Regional Centre of Advanced Technologies and Materials, Department of Physical Chemistry, Faculty of Science, Palacký University, tř. 17 listopadu 12, 771 46, Olomouc, Czech Republic

# ABSTRACT

The widespread manganese-ion sensing *yybP-ykoY* riboswitch controls the expression of bacterial  $Mn^{2+}$  homeostasis genes. Here, we first determine the crystal structure of the ligand-bound *yybP-ykoY* riboswitch from *Xanthomonas oryzae* at 2.85 Å resolution, revealing two conformations with docked four-way junction (4WJ) and incompletely coordinated metal ions. In >50  $\mu s$  of MD simulations, we observe that loss of divalents from the core triggers local structural perturbations in the adjacent docking interface, laying the foundation for signal transduction to the regulatory switch helix. Using single-molecule FRET, we unveil a previously unobserved extended 4WJ conformation that samples transient docked states in the presence of  $Mg^{2+}$ . Only upon adding sub-millimolar  $Mn^{2+}$ , however, can the 4WJ dock stably, a feature lost upon mutation of an adenosine contacting  $Mn^{2+}$  in the core. These observations illuminate how subtly differing ligand preferences of competing metal ions become amplified by the coupling of local with global RNA dynamics.

## INTRODUCTION

Riboswitches are structured RNA motifs commonly found in the 5'-untranslated regions of bacterial mRNAs, where they regulate many essential and virulence genes in response to binding of a specific ligand<sup>1-3</sup>. Currently, there are over 40 different riboswitch classes known to respond to ligands ranging from metabolites<sup>4</sup>, enzyme cofactors<sup>5</sup>, signaling molecules<sup>6-8</sup>, tRNAs<sup>9</sup>, and to metal ions<sup>10-12</sup>. Ligand binding generally stabilizes a conformation of the riboswitch that modulates either Rho-independent transcriptional termination or translation initiation through accessibility of the Shine-Dalgarno (SD) sequence. The static ligand-bound structures, and the ligand-recognition modes, of a number of riboswitches have been determined at atomic resolution<sup>2,12-14</sup>. Often, the ligand occupies a linchpin position in the global fold where distal residues of the RNA are brought together; however, the dynamic paths by which the local binding of a ligand as small as a metal ion are transduced into the large-scale molecular rearrangements necessary for a regulatory decision by the gene expression machinery largely remain enigmatic<sup>14</sup>.

The *yybP-ykoY* RNA motif is one of the most widespread riboswitches across bacteria, including human and plant pathogens<sup>15-17</sup>. It has evolved to sensitively detect  $Mn^{2+}$  metal ions and broadly regulate a variety of genes, particularly those involved in  $Mn^{2+}$  homeostasis, at the levels of either transcription or translation<sup>12,15,18</sup>. We previously solved crystal structures of this riboswitch, suggesting that the charge, geometry, and Lewis-acid hardness of  $Mn^{2+}$  may be sensed locally by encapsulation of the cation by five phosphoryl oxygens and the N7 of a conserved adenosine. The global structure suggested that formation of the binding site requires “docking” of two distal helical legs of a four-way junction (4WJ) to form a paperclip-shaped global architecture, facilitated by an A-minor interaction and a second, nonspecific divalent metal binding site (**Fig. 1a**)<sup>12</sup>. However, the transduction of ligand binding in this metal-sensing core into global structural

changes that affect the distal helix P1.1 involved in riboswitching is not understood, rendering it an archetypical representative of our level of understanding of many crystallized riboswitches<sup>14</sup>.

Here, we first solve the structures of two ligand-bound states of the *yybP-ykoY* transcriptional riboswitch from the rice pathogen *X. oryzae*<sup>19,20</sup>, captured in distinct conformations that offer ‘snapshots’ of structural changes *en route* to full ligand binding. We then use these conformers for atomistic molecular dynamics (MD) simulations that reveal how ligand-dependent local structural perturbations in the metal-sensing core are linked to the stability of distal P1.1 helix to affect riboswitching. Finally, using single-molecule FRET (smFRET), we investigate the global structural dynamics of the riboswitch in the presence of varying concentrations of  $Mg^{2+}$  and  $Mn^{2+}$ , as well as other transition metals, revealing a previously unobserved extended conformation of the riboswitch. We show that addition of  $Mg^{2+}$  induces two kinetically distinct docked conformations that remain in dynamic equilibrium with the extended conformation. In contrast, upon addition of sub-millimolar  $Mn^{2+}$ , the riboswitch adopts a stably docked conformation that becomes abolished upon mutation of the conserved core adenosine. Taken together, our work reveals the ligand-dependent (un)folding pathway of the  $Mn^{2+}$  sensing riboswitch as a guide for how subtle binding preferences distinguishing two similar metal ion ligands cascade through the coupling of local with global RNA conformational dynamics into powerful effects on gene regulation.

## RESULTS

### ***X. oryzae yybP-ykoY* crystal structures reveal disordered metal sensing cores**

We determined the structure of the *yybP-ykoY* riboswitch from *X. oryzae* in the presence of  $Mn^{2+}$  (Xory-Mn) by X-ray crystallography at 2.85 Å resolution (**Fig. 1b and Supplementary Table 1**).

In this phytopathogenic bacterium that causes rice blight, the riboswitch is found upstream of the *yebN*  $Mn^{2+}$  efflux pump gene<sup>20</sup>, whose characterization helped identify the *yybP-ykoY* RNA as a



Mn<sup>2+</sup> riboswitch. To facilitate crystallization, the wild-type (WT) Xory sequence was modified distally from the metal sensing core not to affect metal binding, tightening the 4WJ and stabilizing P1.1 to aid crystallization (see Methods, **Fig. 1a**).

Fortuitously, the resulting Xory-Mn structure contained two different conformations in the same crystal lattice (**Fig. 1c**). The two conformers, termed “1” and “2”, are globally quite similar to each other (overall RMSD = 2.53 Å) and, as expected, to the previously determined *L. lactis* canonical Mn<sup>2+</sup>-bound structure, featuring a dual coaxial stack connected at the top by the 4WJ<sup>12</sup> (**Figs. 1b,c**). As in Llac-Mn, Xory-Mn shows that the conserved L1 and L3 loops dock the two adjacent legs of the 4WJ<sup>12</sup>, wherein L1 forms a sarcin-ricin-like motif (SRL-like) that flips out A10, which forms a cross-helix A-minor interaction with helix P3.1 above L3 (**Fig. 1c**). This non-standard sarcin-ricin loop differs from the canonical loop since A10 is inserted upstream of the G-bulge region (i.e., G9) and the *trans*-Watson-Crick/Hoogsteen base pairing of G9-G93 is distinct from the canonical *trans*-Hoogsteen/Hoogsteen pairing<sup>21</sup>. L3 stacks below A10, orienting its phosphates inward, resulting in a pocket of high negative charge density. Consequently, between the loops two largely dehydrated metal sites are found. In Llac-Mn, the first site, M<sub>A</sub>, is inner-sphere coordinated (at a distance of 2.0-2.3 Å) by five phosphoryl oxygens and a water molecule, and was predicted to be a nonspecific divalent binding site, generally harboring Mg<sup>2+</sup>; we will henceforth refer to it as M<sub>A,Mg</sub>. The second site, M<sub>B</sub>, is coordinated by five phosphoryl oxygens and the N7 of a highly conserved adenosine A41 in L3, which – through its “soft” coordination – appears to help specify Mn<sup>2+</sup> as the preferred metal ion ligand<sup>12</sup> (**Fig. 1d**); we will henceforth refer to it as M<sub>B,Mn</sub>. The two new structures each contain both of these ions, and thus support our previous analysis<sup>12</sup>. Of note, we used 80 mM SrCl<sub>2</sub> and 20 mM MgCl<sub>2</sub> in the crystallization and, based on the anomalous signal obtained near the Sr K-edge wavelength (0.769 Å), there is no or

little  $\text{Sr}^{2+}$  occupancy at either of the  $\text{M}_{\text{A,Mg}}$  or  $\text{M}_{\text{B,Mn}}$  sites compared to external sites in the structure, attesting to specificity for the smaller divalent ions.

While the two new Xory-Mn conformers are similar, the regions immediately surrounding the metal ion binding sites differ between them and Llac-Mn. The Conformer 1'  $\text{M}_{\text{B,Mn}}$  binding area is most similar to the *L. lactis*  $\text{M}_{\text{B,Mn}}$ , except U49 in the L3 backbone is flipped out, away from the stacked conformation observed for the equivalent *L. lactis* A42 (**Fig. 1d, Supplementary Fig. 2**), while still preserving all  $\text{M}_{\text{B,Mn}}$  metal contacts (**Fig. 2a**). By comparison, the conformer 1  $\text{M}_{\text{A,Mg}}$  site is more distinct in that the inner-sphere contacts to the phosphoryl oxygens of G8 and A10 are lost (shown as red lines), with G8 potentially retaining an outer-sphere, through-water contact (**Fig. 2a**).

Compared to Conformer 1, Conformer 2 exhibits even more pronounced changes. While both metal ions remain bound, L3 is shifted away from P1.1. As a consequence, the  $\text{M}_{\text{A,Mg}}$  site in Conformer 2 has lost one metal contact, that to U52 in L3, consistent with this loop's shift. The  $\text{M}_{\text{B,Mn}}$  site is concomitantly moved by 2 Å relative to its position in Llac-Mn and Conformer 1 (**Fig. 1d**). Three of its metal contacts are lost, specifically the inner-sphere contacts to the phosphates of C51, U52, and G9, which are now too far to interact at 6.8, 5.8, and 4.4 Å, respectively (**Fig. 2b**). Two of these lost contacts, U52 and G9, are from phosphates that bridge the two metal sites. Interestingly, the electron density is sufficiently clear to suggest that A48 in the binding site is flipped relative to its previous orientation, now orienting its N1, rather than N7, toward  $\text{M}_{\text{B,Mn}}$ . Consistent with this generally disorganized architecture, the temperature B-factors for L3 are higher in Conformer 2 than Conformer 1 (**Fig. 2c,d**), indicating increased flexibility. Strikingly, this includes larger flexibility around P1.1, suggesting a possible link between the flexibilities of these two key regions. Taken together, our crystal structures provide first evidence

that lost contacts between the metal ions, L1, and a partially unfolded L3 can translate into disorder in the distal P1.1 helix, which provides a basis for riboswitching.

## **MD simulations reveal effects of $M_{A,Mg}$ and $M_{B,Mn}$ inner-sphere contacts on L3 stacking**

To provide deeper insights into the RNA dynamics associated with metal identity, we performed 29 atomistic molecular dynamics (MD) simulations, equivalent to a total of 53  $\mu$ s of real-time (see **Table 1, Methods**), with different metal ions in the  $M_{A,Mg}$  and  $M_{B,Mn}$  sites and starting either from Xory-Mn Conformers 1 or 2 (as reported here) or from Llac-Mn. As expected, given their necessarily limited timescales compared to experiments<sup>22,23</sup>, we found that our simulations generally maintained quite stable inner-sphere contacts for divalent metal ions, including their coordination with water molecules (**Fig. 3a-c**). To accelerate these dynamics we performed additional MD simulations that replaced one or both divalent ions at the  $M_{A,Mg}$  and  $M_{B,Mn}$  ion binding sites with monovalent  $K^+$  ions (**Table 1**). Importantly, while the divalent-to-monovalent replacement affects both the thermodynamics and kinetics of the inner-sphere contacts of the metal ions, their relative thermodynamic stability allows monovalent first-shell ligands to model the functional behavior of divalents on a shorter timescale<sup>22,23</sup>. Accordingly, even these more dynamic simulations maintained the global architecture of the riboswitch except for local perturbations of L3 and a variable P2-P4 helical angle (**Supplementary Fig. 4 and Supporting Information**).

Upon closer inspection, we found that the inner coordination sphere of monovalent ions in both the  $M_{A,Mg}$  and  $M_{B,Mn}$  sites were significantly more stable in simulations where the second binding site was occupied by a divalent rather than monovalent ion (**Fig. 3a**). This observation suggests that binding of the divalent ion into one binding site may help pre-organize and stabilize

the second binding site, consistent with the notion of cooperativity between  $M_{A,Mg}$  and  $M_{B,Mn}$ . Furthermore, while some inner-sphere contacts remained very stable, other contacts were lost upon replacement with a monovalent (**Fig. 3a-c**). Notably, the bridging inner-sphere contacts of the U52 phosphate with the  $M_{A,Mg}$  ion and those of the C51 and G9 phosphates with the  $M_{B,Mn}$  metal were found to be most labile across all simulations (**Fig. 3a, Supplementary Table 2 and Supplementary Figs. 4,5**). These are the same inner-sphere contacts found to be lost in the crystallized Conformers 1 and 2 compared to the Llac-Mn, supporting the notion that the Conformers are relevant *en route* to (un)folding of the metal ion binding sites. In contrast, the inner-shell contacts of the A46 phosphate with the ions in both  $M_{A,Mg}$  and  $M_{B,Mn}$ , as well as those of the G9 phosphate with the ion in  $M_{A,Mg}$  and of the C47 phosphate with the ion in  $M_{B,Mn}$ , were stable across all simulations (**Fig. 3a, Supplementary Table 2 and Supplementary Figs. 4,5**). These latter interactions are likely stabilized by coupling of the A-minor interaction of A10 to the G66-C44 base pair and associated stacking of A10 on the neighboring A46. All these interactions are parts of the L1-L3 tertiary docking contact and remained stable across all simulations (**Fig. 3d**).

We also found the dynamics of the entire L3 loop to be sensitive to the type of ion in the  $M_{B,Mn}$  site. When  $Mn^{2+}$  in the  $M_{B,Mn}$  site was replaced with  $K^+$ , the flexibility of the L3 loop was increased so that the loop populated various conformations with broken stacking patterns (**Fig. 3b and Supporting Information**). These perturbations originated from the weakened inner-sphere contact of the A48(N7) nitrogen to the  $M_{B,Mn}$  metal, suggesting that the L3 loop is involved in direct sensing of the  $Mn^{2+}$  ion by forming a linchpin to support a tight stacking patterns only in the presence of the native  $Mn^{2+}$  (**Fig. 3e**).

## Stability of the SRL-like conformation of L1 loop requires an A-minor interaction

To complement our probing of structural dynamics in the docked state with those in the undocked state, we performed additional MD simulations of the segment consisting only of P1.1, P1.2 and L1. We started these “undocked” simulations from either of the two Xory-Mn Conformers and Llac-Mn (**Table 1**), with the aim to reveal their structural dynamics in the absence of the L1-L3 docking contact. While the L1 loop in the context of the entire riboswitch with its docked L1-L3 interaction always populated the SRL-like, two of our three “undocked” simulations lost this motif (**Figs. 3f,g, Supplementary Fig. 8, and Supporting Information**). In particular, in one of the simulations we observed loss of the G9-G93 *trans* Watson-Crick/Hoogsteen and G8-A94 *trans* Sugar-Edge/Hoogsteen base pairing<sup>21</sup> as well as the S-turn<sup>24</sup> that forms part of the M<sub>A,Mg</sub> site (**Fig. 3f,g**). The former two base pairs are coaxially stacked on the P1.1 stem, suggesting that their loss may highlight the beginning of a transduction path by which P1.1 could become destabilized.

## smFRET reveals an undocked conformation that transiently docks upon Mg<sup>2+</sup> addition

To probe the global structural dynamics in the presence of Mg<sup>2+</sup> and Mn<sup>2+</sup>, we used smFRET to monitor fluorophores positioned on the distal legs of the Xory riboswitch (**Fig. 4a, Supplementary Fig. 13, and Methods**). smFRET traces at 100 mM KCl in the absence of any divalent metal ions showed a stable low-FRET value of ~0.1 without global dynamics (**Fig. 4b**), with a population FRET histogram displaying a single peak centered on ~0.13±0.10 (mean ± standard deviation) (**Fig. 4c**). The non-dynamic nature of the traces is also evident as an ‘on-diagonal’ contour centered at ~0.13 in the transition occupancy density plot (TODP), which shows initial vs. final FRET value transitions for the population of molecules as a heat map (**Fig. 4d**). This FRET value corresponds to an estimated distance of ~74 Å between the two fluorophores and suggests an extended, stably

undocked (SU) conformation where the two RNA legs are distal and do not interact, unlike the docked crystal structure (**Fig. 1b**).

Addition of  $\text{Mg}^{2+}$  up to 0.1 mM did not result in significant changes in the FRET histograms since almost all traces remained in the SU conformation, with  $\sim 3\%$  of them showing brief excursions into a higher  $\sim 0.6$ -FRET state (**Supplementary Fig. 14**). Further raising the  $\text{Mg}^{2+}$  concentration resulted in more dynamic traces transiently adopting this high-FRET state, accompanied by a corresponding decrease in the population of SU traces (**Fig. 4b-d**, **Supplementary Fig. 14**). At a near-physiological concentration of 1 mM  $\text{Mg}^{2+}$ , the time- and population-averaged distribution between low- and high-FRET, with mean FRET values of  $\sim 0.15 \pm 0.11$  (49 %) and  $0.63 \pm 0.14$  (51 %), respectively, became almost equal (**Fig. 4c**). A FRET value of 0.63 corresponds to a distance of  $\sim 49$  Å between the two labeled RNA arms, similar to the distance observed in the crystal structures, suggesting adoption of the compact ‘docked’ conformation. Reaching 10 mM  $\text{Mg}^{2+}$ , the fraction of this docked conformation further increased and saturated at  $\sim 69\%$ , with a sigmoidal  $\text{Mg}^{2+}$  concentration dependence that fit well with a Hill equation to yield a half-saturation point of  $K_{1/2} \sim 0.6$  mM and a cooperatively coefficient of  $n = 1.7$  (**Fig. 4e**). These data demonstrate that the  $\text{Mn}^{2+}$  riboswitch adopts an extended SU conformation in the absence of divalents, which increasingly samples transient docked conformations upon a rise in  $\text{Mg}^{2+}$  concentration.

At a low  $\text{Mg}^{2+}$  concentration of 0.1 mM, single-exponential kinetics were observed with a slow docking rate constant,  $k_{\text{dock}} \sim 0.56 \text{ s}^{-1}$ , and a fast undocking rate constant,  $k_{\text{undock}} \sim 12.5 \text{ s}^{-1}$  (**Fig. 4f** and **Supplementary Fig. 15**). Further increasing the  $\text{Mg}^{2+}$  concentration to 1 mM resulted in the emergence of double-exponential kinetics in both  $k_{\text{dock}}$  and  $k_{\text{undock}}$ . The docking kinetics exhibited  $k_{\text{dock}}^{\text{fast}} \sim 6.25 \text{ s}^{-1}$  and  $k_{\text{dock}}^{\text{slow}} \sim 0.76 \text{ s}^{-1}$ , while the undocking kinetics displayed  $k_{\text{undock}}^{\text{fast}}$

$\sim 3.70 \text{ s}^{-1}$  and  $k_{undock}^{slow} \sim 1.21 \text{ s}^{-1}$  (**Fig. 4f and Supplementary Fig. 15**). The TODP further shows that a majority (82 %) of traces are dynamically transitioning between the two FRET states, as highlighted by dominant ‘off-diagonal’ contours, while only a small fraction ( $\sim 18$  %) remains in the stable low-FRET state (**Fig. 4d**). The double-exponential kinetics arises from two distinct populations: ‘dynamic docked’ (DD) and ‘dynamic undocked’ (DU) traces corresponding to molecules residing largely in the docked and undocked states, respectively. (**Fig. 4g**). Among the dynamic traces,  $\sim 65$  % were DD while  $\sim 35$  % were DU traces. As observed for other RNAs that undergo docking of two adjacent helical arms<sup>25-31</sup>, the heterogeneity observed in the population was largely static and molecular behaviors interconverted only rarely ( $< 2\%$  of traces) over the experimental timescale (5-10 min) (**Fig. 4h**). Interconversion between the DU and DD behaviors was observed more readily, however, when first chelating, then reintroducing  $\text{Mg}^{2+}$  (**Fig. 4i**), suggesting that they represent kinetically trapped conformations on a deeply rugged folding free energy landscape<sup>32,33</sup>.

### **Sub-millimolar $\text{Mn}^{2+}$ uniquely yields a stably docked riboswitch**

We next asked what specific effect  $\text{Mn}^{2+}$  has on the folding of the riboswitch. In the presence of 1 mM  $\text{Mg}^{2+}$ , addition of a low concentration of 0.1 mM  $\text{Mn}^{2+}$  resulted in the appearance of a unique population of stably docked (SD,  $\sim 43\%$ ) traces residing in the high-FRET state for  $> 30 \text{ s}$  ( $k_{undock} < 0.03 \text{ s}^{-1}$ ) before photobleaching (**Fig. 5a**). Accordingly, the FRET histogram showed two peaks with mean FRET values of  $0.17 \pm 0.14$  and  $0.69 \pm 0.12$  and an increased  $\sim 68$  % population of the docked conformation (**Fig. 5a**). The SD population is evident in the TODP as a new ‘on-diagonal’ contour centered on the  $\sim 0.7$ -FRET value (**Fig. 5a**). Dynamic traces under these conditions again showed double-exponential behavior and were similar to the kinetics at 1 mM  $\text{Mg}^{2+}$  alone, with  $k_{dock}^{fast} = 5.55 \text{ s}^{-1}$ ,  $k_{dock}^{slow} = 0.46 \text{ s}^{-1}$ ,  $k_{undock}^{fast} = 3.84 \text{ s}^{-1}$  and a  $\sim 5$ -fold slower  $k_{undock}^{slow}$  of  $0.23 \text{ s}^{-1}$ .

Notably, in the presence of  $\text{Mn}^{2+}$ , most of the dynamic traces now showed DD character. These data demonstrate that  $\text{Mn}^{2+}$  binding generally stabilizes the docked conformation while uniquely enabling a new, stably docked SD state. FRET histograms further showed that out of a variety of divalent metal ions tested, only  $\text{Cd}^{2+}$  is effective in promoting docked conformations over just 1 mM  $\text{Mg}^{2+}$  alone;  $\text{Ni}^{2+}$ ,  $\text{Co}^{2+}$ ,  $\text{Sr}^{2+}$  or  $\text{Zn}^{2+}$  had little effect (**Fig. 5b**, **Supplementary Fig. 16**). Interestingly, in the absence of  $\text{Mg}^{2+}$ , while 0.1 mM  $\text{Mn}^{2+}$  alone led to the appearance of DD and SD traces with ~62 % docked population (mean FRET  $0.67 \pm 0.12$ ) (**Fig. 5c**), 0.1 mM of  $\text{Ni}^{2+}$ ,  $\text{Co}^{2+}$ ,  $\text{Sr}^{2+}$  or  $\text{Zn}^{2+}$  did not affect SU traces and  $\text{Cd}^{2+}$  had only a small effect in promoting DD traces. These results suggest that while the *Xory* riboswitch has some degree of plasticity in recognizing ligands, in a background of  $\text{Mg}^{2+}$  it preferentially recognizes  $\text{Mn}^{2+}$  and – to a lesser extent –  $\text{Cd}^{2+}$ .

To probe how the kinetically distinct SU, DU and DD traces respond to  $\text{Mn}^{2+}$ , we observed the same set of molecules at 1 mM  $\text{Mg}^{2+}$  before and after the addition of  $\text{Mn}^{2+}$ . We found that all three populations respond to  $\text{Mn}^{2+}$  and are capable of forming the stably docked (SD) population (**Fig. 5d**). In particular, the SU traces converted into DU, DD, and SD conformations with similar probabilities, suggesting that they are correctly folded with metal sensing sites poised to bind ligand. By comparison, a majority of DD traces converted into SD traces whereas DU traces adopted DD and SD behavior upon  $\text{Mn}^{2+}$  addition. Only a small fraction of traces showed no response at low  $\text{Mn}^{2+}$  suggesting that they may be misfolded.

### **Mutation of the conserved adenosine A48 results in complete loss of the SD conformation**

The highly conserved discriminator base A48 in L3 is positioned to confer  $\text{Mn}^{2+}$  specificity via its N7 and also helps maintain L3 in a stacked conformation. We therefore tested the effect of a single A48U mutation on folding and  $\text{Mn}^{2+}$  sensing of the riboswitch. Similar to the WT, at 100 mM KCl



without divalents, smFRET traces of the mutant riboswitch showed the SU population with a mean FRET value of  $0.11 \pm 0.12$  (**Fig. 5e**). At 1 mM  $\text{Mg}^{2+}$ , we observed dynamic traces with excursions into the docked higher FRET states, and the FRET histogram showed a major (64 %)  $0.14 \pm 0.11$  low-FRET peak and a minor (36 %) broad  $0.52 \pm 0.21$  mid-FRET peak that corresponds to more extended docked conformations (**Fig. 5f**). Of note, 100% of the dynamic mutant traces showed DU character with only brief excursions into the docked conformations (**Fig. 5f**). As a result, we observed fast single-exponential undocking with  $k_{\text{undock}} \sim 6.67 \text{ s}^{-1}$  while  $k_{\text{dock}}$  was double-exponential with a major  $k_{\text{dock}}^{\text{fast}} = 3.70 \text{ s}^{-1}$  (95 %) and a minor  $k_{\text{dock}}^{\text{slow}} = 0.46 \text{ s}^{-1}$  (5 %) (**Supplementary Fig. 17**). The TODPs show SU behavior in the absence of divalents, whereas both SU and DU behaviors are observed at 1 mM  $\text{Mg}^{2+}$  (**Fig. 5e,f**).

Next, we asked whether the mutant riboswitch can still respond to  $\text{Mn}^{2+}$ . In the presence of 1 mM  $\text{Mg}^{2+}$  and 0.1 mM  $\text{Mn}^{2+}$ , most smFRET traces were dynamic and showed DD behavior, while only a small fraction remained in the SU state, similar to WT (**Fig. 5g**). FRET histograms show a similar  $\sim 0.14 \pm 0.13$  (57 %) low-FRET undocked state but display a docked state now with a higher mean-FRET value of  $0.63 \pm 0.15$  and a larger  $\sim 43$  % population (**Fig. 5g**), compared to the 1 mM  $\text{Mg}^{2+}$  only condition. . The kinetics under these conditions were double-exponential with a  $k_{\text{dock}}^{\text{fast}} = 6.67 \text{ s}^{-1}$  (89 %),  $k_{\text{dock}}^{\text{slow}} = 0.64 \text{ s}^{-1}$  (11 %),  $k_{\text{undock}}^{\text{fast}} = 3.10 \text{ s}^{-1}$  (94 %),  $k_{\text{undock}}^{\text{slow}} = 0.88 \text{ s}^{-1}$  (6 %) (**Supplementary Fig. 17**). Importantly, the mutation caused a striking loss of SD traces, as evident from the complete absence of the on-diagonal  $\sim 0.7$  FRET contour in the TODP (**Fig. 5g**), in stark contrast to the WT. In addition, the mutant interestingly loses the WT's ability to sample the docked conformations in the presence of 0.1 mM  $\text{Mn}^{2+}$  alone (**Fig. 5g**); almost all smFRET traces at 0.1 mM  $\text{Mn}^{2+}$  are in the SU conformation, with the histogram showing a major single peak around  $0.19 \pm 0.13$  FRET, further corroborated by a single on-diagonal  $\sim 0.2$  FRET contour in

the TODP (**Fig. 5h**). These data demonstrate that the conserved discriminator A48 is essential for  $Mn^{2+}$  inducing a stably docked riboswitch conformation. The presence of  $Mg^{2+}$  partially rescues the loss of  $Mn^{2+}$  sensing by the mutant, yet does not restore its ability to form the SD conformation. Possibly this reflects the ability of  $Mg^{2+}$  to bind at  $M_B$  in A48U, though with weaker affinity, via the uridine O4, as suggested in the A41U *L. lactis* structure<sup>12</sup>.

## DISCUSSION

Using a combination of X-ray crystallography, MD simulations and smFRET, our work here sheds light on how the binding of a single  $Mn^{2+}$  ion can modulate the stability of the distant switch helix through a conformational cascade that couples local with global structural dynamics. While previous structures revealed the local  $Mn^{2+}$  recognition mechanism of *yybP-ykoY* RNA<sup>12</sup>, the new structures reported here underscore the conformational plasticity around the metal binding core. Importantly, the structural differences observed between the two conformers in the crystal lead us to posit that Conformer 2 with L3 partially unfolded around  $M_{B,Mn}$  is likely an intermediate between the fully  $Mn^{2+}$ -bound state and the empty  $M_{B,Mn}$  state observed in the *E. coli*  $Mn^{2+}$ -free structures<sup>12</sup>. We hypothesize that the loss of phosphate contacts from C51, U52, and G9 to  $Mn^{2+}$  in Conformer 2 reflects their relative weakness as supported by MD simulations and likely represents a discrete step in  $Mn^{2+}$  binding/unbinding. Conversely, the variation in  $M_{B,Mn}$  site coordination we observe could represent inherent flexibility at this site, allowing it to recognize  $Mn^{2+}$  even if the metal ion is not fully dehydrated. This flexibility is also seen in the recent  $Cd^{2+}$ -bound structures (see **Supporting Information**).

Our MD simulations show that the SRL-like motif in L1 is inherently unstable in the L1-L3 undocked state, but is stabilized by the tertiary A-minor interaction of A10 with P3.1. Similarly,

L1-L3 docking stabilizes L3 in a stacked conformation by direct stacking of A10 on top of it. Thus, a stable conformation of L1 and therefore P1.1 is intimately linked to the stability of L3 and the tertiary A-minor interaction. We suggest that the SRL-like motif acts as a molecular switch that links the  $Mn^{2+}$ -dependent increase in docking observed by smFRET to stabilization of P1.1.

Using smFRET we further identify a globally undocked conformation at physiological  $Mg^{2+}$  concentration that remains in dynamic equilibrium with the compact docked conformations. In fact, the observation of pairs of stably and dynamically docked and undocked states with double-exponential docking and undocking kinetics supports the existence of at least two undocked and docked dynamic (in addition to the static SU and SD) conformations, with similar FRET values and thus global folds, but likely different local conformations around the ligand sensing core. These conformations are possibly related to Conformers 1 and 2 in the crystal structure. We further find that SD conformations are formed only in the presence of sub-millimolar  $Mn^{2+}$  or the related soft transition metal  $Cd^{2+}$ , and lost upon a single mutation of the invariant  $Mn^{2+}$ -sensing adenine A48.

Our structural snapshots, MD simulations and smFRET data support the model shown in **Fig. 6**. In the absence of any divalent ions, the *Xory* riboswitch adopts an extended conformation in which the two legs are distal and rarely interact, as shown by smFRET. Under these conditions, the metal-binding sites are likely unstructured and their interaction only transiently formed by L1-L3 contacts, as suggested by rare smFRET transitions, MD simulations as well as previous ligand-free structures<sup>12</sup>. Our MD simulations in particular show that the A-minor interaction formed by A10 of L1 loop with the GC base pair of stem P3.1 can at least transiently form even in the absence of divalents. The formation of this A-minor interaction helps pre-organize the  $M_{A,Mg}$  binding site. Under physiological (1 mM) concentrations of  $Mg^{2+}$ , this ion binds first at the  $M_{A,Mg}$  site, allowing

the riboswitch to sample dynamic folded conformations where the two legs are brought together via metal-mediated interaction between loops L1 and L3. These dynamic folded states then allow for local interactions mediated by L3, forming a pocket of high negative charge potential poised to sense  $Mn^{2+}$ .  $Mg^{2+}$  binding at  $M_{A,Mg}$  therefore facilitates binding of  $Mn^{2+}$  at  $M_{B,Mn}$  in cooperative fashion, as shown by smFRET at the global level and further visualized by atomistic MD simulations. Capture of  $Mn^{2+}$  at site  $M_{B,Mn}$  then acts as the final linchpin to hold the two legs together most stably. This compact docked conformation with a SRL-like fold of L1 and continuous coaxial stacking between P1.2, L1 and P1.1 stabilizes the remote P1.1 ‘switch’ helix and prevents the strand invasion required to form the terminator hairpin, instead promoting transcriptional read-through.

Contrasting with the  $Mn^{2+}$  riboswitch, the NiCo riboswitches, which cooperatively sense the transition metals  $Ni^{2+}$  or  $Co^{2+}$ , resemble the overall ‘H’ shaped architecture of the  $Mn^{2+}$  riboswitch but with a tight 4WJ that lacks an analogous tertiary docking interface. Accordingly, the NiCo riboswitch appears to act through a distinct mechanism utilizing four bound metal ions to weave together a network of interactions between the interhelical residues that stabilize the 4WJ and so prevent formation of a terminator via strand invasion<sup>34</sup>. Similarly, the  $Mg^{2+}$  sensing M-box riboswitch adopts an architecture with three parallel co-axially stacked helices that are brought together by the binding of six  $Mg^{2+}$  ions, leading to formation of a terminator<sup>35</sup>. Therefore, both the NiCo and  $Mg^{2+}$  sensing riboswitches achieve gene regulation by employing multiple metal ions that directly interact with and stabilize the ‘switch’ helix. The  $Mn^{2+}$  riboswitch is thus unique in requiring only a single metal ion that does not make any direct contacts with switch helix P1.1. By combining high-resolution structural information with insights into both atomistic and global dynamics, our study outlines the mechanism by which a ligand as small as a single divalent metal

ion couples local with global structure to give  $Mn^{2+}$  the ability to influence RNA folding and fine-tune gene expression by cooperating with a high background of  $Mg^{2+}$ . The general lessons revealed here of how a ligand-binding signal can be transduced across an RNA are likely to become a recurring theme among riboswitches where the ligand represents a distal structural linchpin for the ‘switch’ helix.

## Acknowledgements

This work was supported by NIH R01 grants GM062357 and GM118524 to N.G.W., by project SYMBIT reg. number CZ.02.1.01/0.0/0.0/15\_003/0000477 funded by the ERDF (M.J. and J.S.), by grant 18-25349S (P.B., P.K.) from the Grant Agency of the Czech Republic, and a student project of Palacky University Olomouc IGA\_PrF\_2018\_032 (M.J.). We thank Qian Hou for help with some experiments. This work included research conducted at NE-CAT beamlines, which are funded by the National Institute of General Medical Sciences from the National Institutes of Health (P30 GM124165). The Pilatus 6M detector on 24-ID-C beam line is funded by a NIH-ORIP HEI grant (S10 RR029205). This research used resources of the Advanced Photon Source, a U.S. Department of Energy (DOE) Office of Science User Facility operated for the DOE Office of Science by Argonne National Laboratory under Contract No. DE-AC02-06CH11357.

## Suddala, Price et al., Figure 1

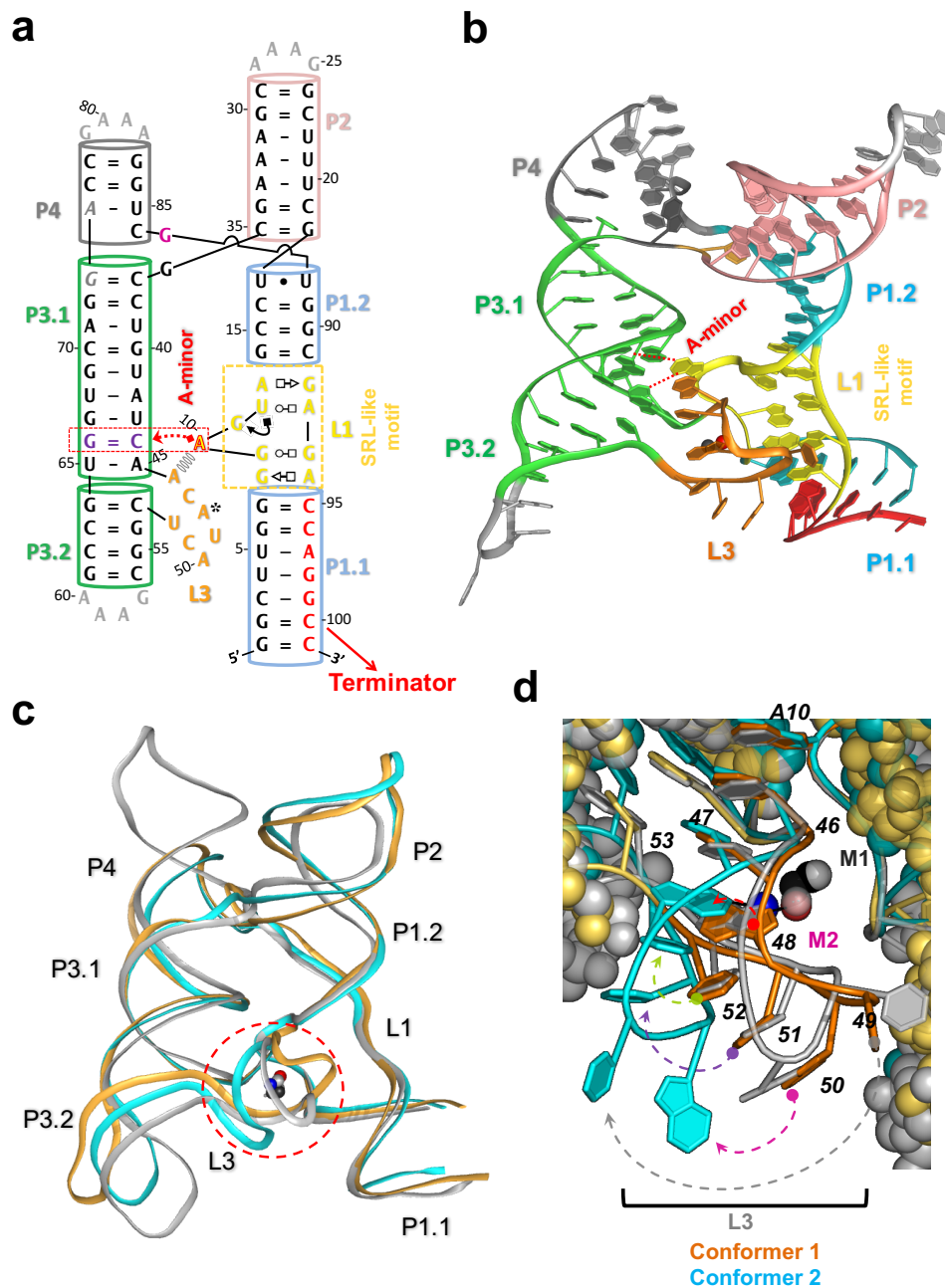


**Figure 1| Sequence and crystal structure of the *X. oryzae* (Xory) *yybP-ykoY*  $Mn^{2+}$  riboswitch.** (a) Sequence and secondary structure of the *X. oryzae* *yybP-ykoY* RNA crystal construct. A native CA dinucleotide was omitted between G73-A74 (gray italics) for crystallization purposes only. The A-minor interaction between L1 and L3 and the SRL-like conformation of L1

are highlighted. **(b)** Crystal structure of Conformer 1 showing the global tertiary fold of the riboswitch along with different secondary structures. **(c)** Comparison of overall structures of Conformers 1 (orange) and 2 (cyan). The two molecules in the asymmetric unit are overall fairly similar. However, they differ dramatically at the metal binding sites (dotted circle). The *L. lactis* structure (gray) is overlaid for comparison. **(d)** Conformer 1 (orange) is relatively similar to the *L. lactis* structure at the  $M_{B,Mn}$  binding site. All the same metal contacts are made, although U49, away from the  $Mn^{2+}$  site, is shifted (gray dotted arrow). Conformer 2 (cyan) differs in that a metal is still bound at the  $M_{B,Mn}$  site, but only half of the metal contacts are made, and the binding site A48 is flipped (red dotted arrow) to expose N1 rather than N7. U49 (gray arrow), A50 (magenta arrow), C51 (purple arrow), and U52 (green arrow) are all significantly shifted from the previously-reported  $Mn^{2+}$ -bound conformation.

## Suddala, Price et al., Figure 2

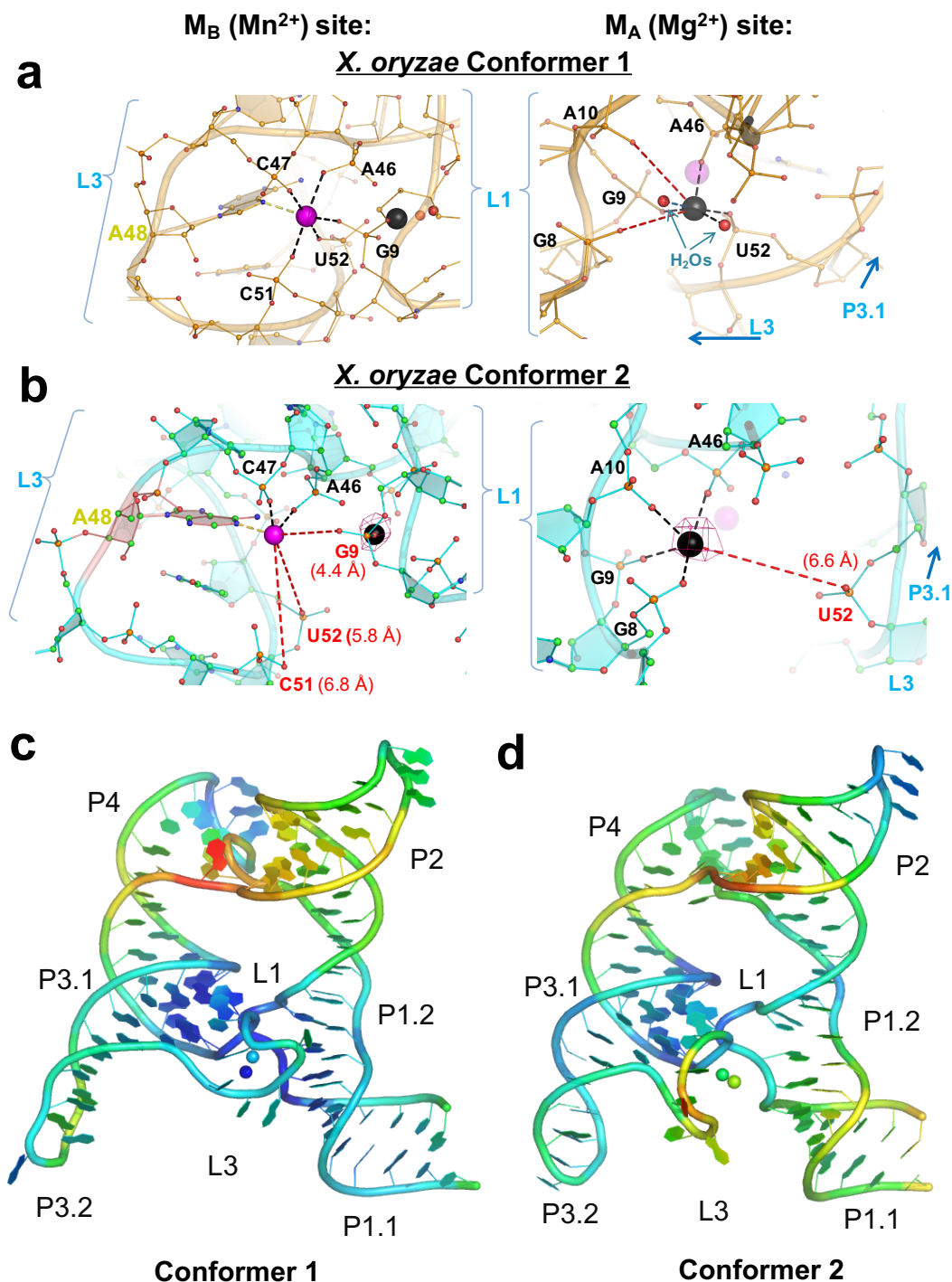


**Figure 2| Conformational differences in the metal binding sites and B-factors in the structures. Close-up view of the M<sub>A,Mg</sub> (black) and M<sub>B,Mn</sub> (purple) metal binding sites of (a)**



Conformer 1 and **(b)** Conformer 2 showing different contacts with surrounding L1 and L3 residues. Waters are shown as red spheres. The lost metal contacts are shown as red dashed lines with their distances. The anomalous difference map at  $4\sigma$  (magenta mesh) shows that  $\text{Sr}^{2+}$  is not observed in Conformer 1 and weakly occupies the  $M_A$  site but not the  $M_B$  site in Conformer 2. Overall *X. oryzae* Conformer 1 **(c)** and Conformer 2 **(d)** structures, colored by individual atomic temperature B-factors (range 38-135  $\text{\AA}^2$  for Conformer 1, 44-170  $\text{\AA}^2$  for Conformer 2). Notice both are well-structured in L1 and in P3 around the binding site. However, Conformer 1 is much more tightly structured in L3 than is Conformer 2. Also, the metal ions in Conformer 1 are somewhat less variable. In both molecules, there is flexibility around the 4WJ.

# **Suddala, Price et al., Figure 3**

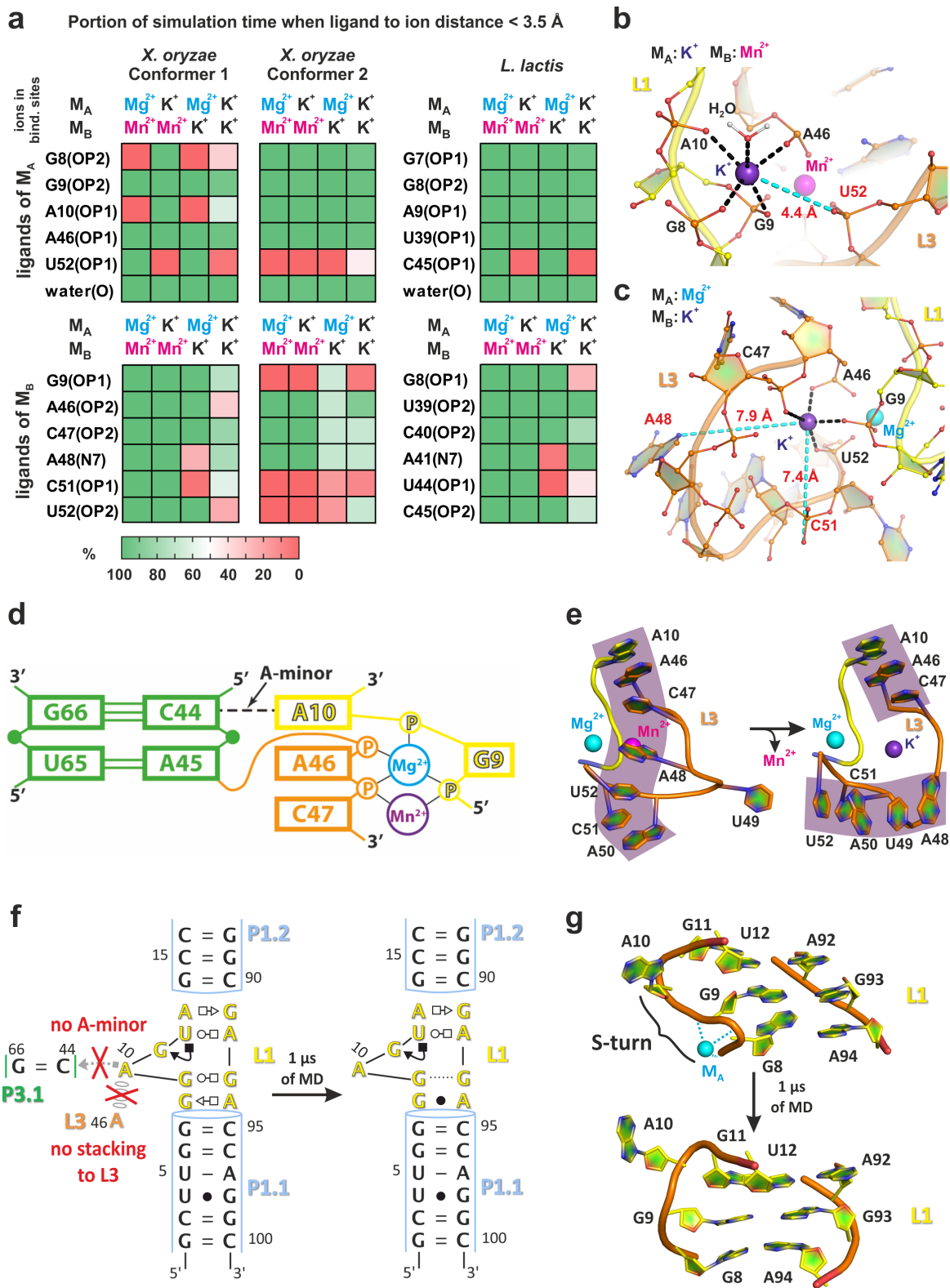


**Figure 3| Structural dynamics of inner-shell ligands of the  $M_{A,Mg}$  and  $M_{B,Mn}$  sites, L3 and L1 loops as revealed by MD simulations.** (a) The population of native inner-shell contacts in the  $M_{A,Mg}$  and  $M_{B,Mn}$  sites in percent as a function of the type of ion in these sites. A representative structure of the (b)  $M_{A,Mg}$  and (c)  $M_{B,Mn}$  site as typically observed in MD simulations with a  $K^+$  ion occupying the site. The most labile inner-shell contacts are depicted in cyan. (d) 2D representation of the most stable part of the L1-L3 tertiary interaction that is likely anchored by the A-minor interaction and related A10|A46 stacking. (e) Partial unfolding of the stacking pattern in the L3 loop observed upon replacement of  $Mn^{2+}$  with  $K^+$  in the  $M_{B,Mn}$  site. (f) The loss of native G9-G93 *trans* Watson-Crick/Hoogsteen and G8-A94 *trans* Sugar-Edge/Hoogsteen base pairing, and (g) loss of the S-turn backbone conformation involving a phosphate notch forming part of the  $M_{A,Mg}$  ion binding site in response to loss of the L1-L3 tertiary interaction with its A10...G66=C44 A-minor interaction.

# **Suddala, Price et al., Figure 4**

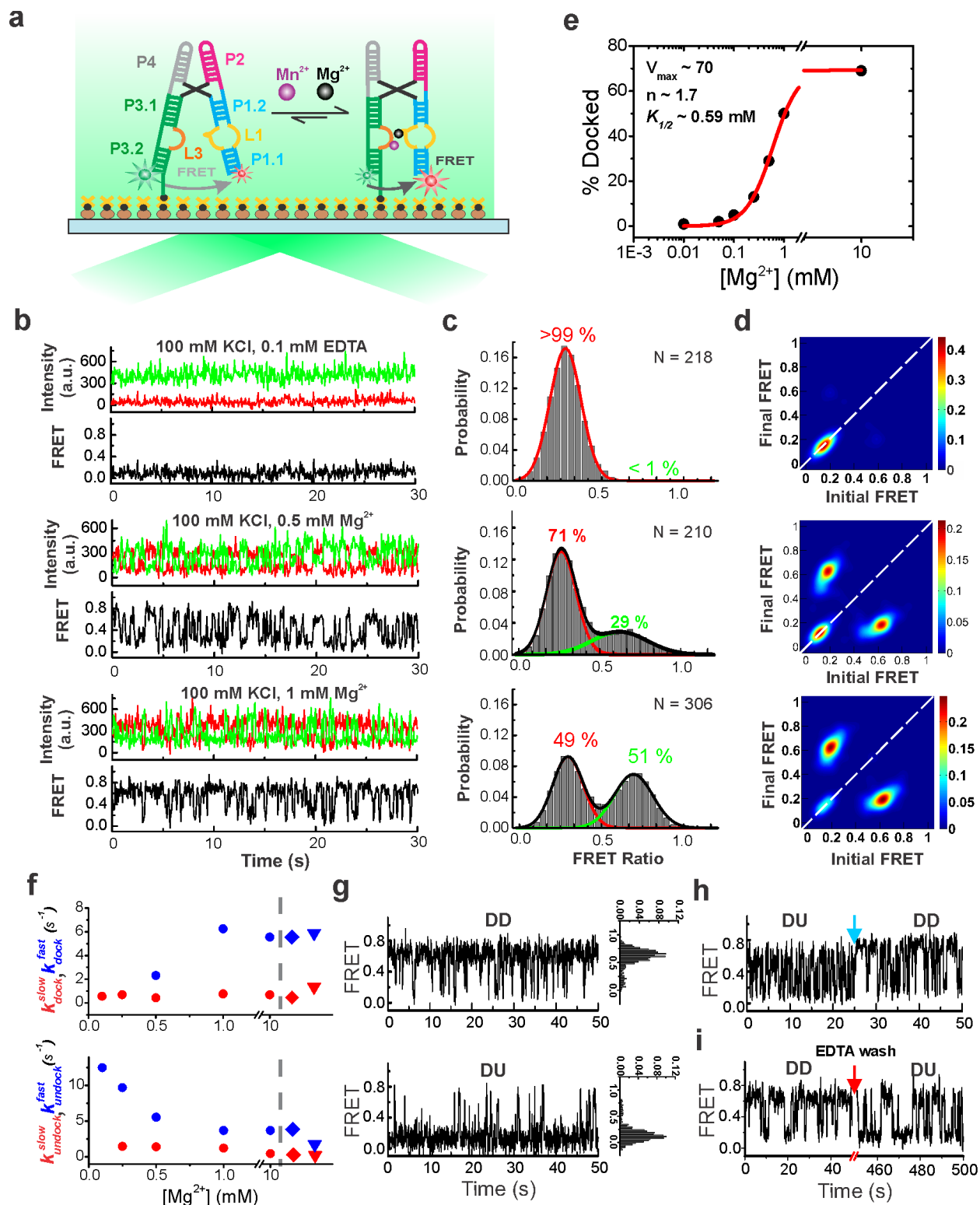


**Figure 4| smFRET analysis of the WT *Xory*  $\text{Mn}^{2+}$  riboswitch.** (a) Schematic of the smFRET experiment using TIRFM indicating the fluorophore labeling positions on the riboswitch. (b) Representative smFRET traces under different buffer conditions (top - bottom): absence of divalents (+0.1 mM EDTA), 0.5 mM  $\text{Mg}^{2+}$  and 1 mM  $\text{Mg}^{2+}$ , respectively. Green, Cy3; Red, Cy5; Black, FRET. (c) Population FRET histograms showing the equilibrium distribution of two FRET states under the conditions of panel (b). Gaussian peaks for the low- and high-FRET states are shown in red and green, respectively with the cumulative fit shown in black. Reported are the percentages of FRET states at equilibrium, as well as the number of molecules N analyzed. (d) TODPs showing the 'static' and 'dynamic' trances as 'on-diagonal' and 'off-diagonal' heat map contours, respectively. The color code indicates the fraction of each population. (e) Fraction of the high-FRET state as a function of  $\text{Mg}^{2+}$  concentration, fit with a standard Hill equation (black). (f) Kinetics of structural dynamics as a function of  $\text{Mg}^{2+}$  and  $\text{Mn}^{2+}$  concentration. The diamond symbols represent rates in 1 mM  $\text{Mg}^{2+}$  and 0.1 mM  $\text{Mn}^{2+}$  while the triangle symbols represent rates in 0.1 mM  $\text{Mn}^{2+}$  alone. (g) Exemplary dynamic docked (DD, top) and dynamic undocked (DU, bottom) traces in the presence of 1 mM  $\text{Mg}^{2+}$ . FRET histograms for the individual traces are shown on the right. (h) Rare examples of interconversion between different kinetic regimes showing dynamic heterogeneity. The blue arrow indicates the time of switching between the two kinetic regimes. (i) Exemplary trace showing conversion of a DU trace to DD trace upon chelation of  $\text{Mg}^{2+}$  with EDTA (indicated by the red arrow) and reintroducing 1 mM  $\text{Mg}^{2+}$ .

# **Suddala, Price *et al.*, Figure 5**

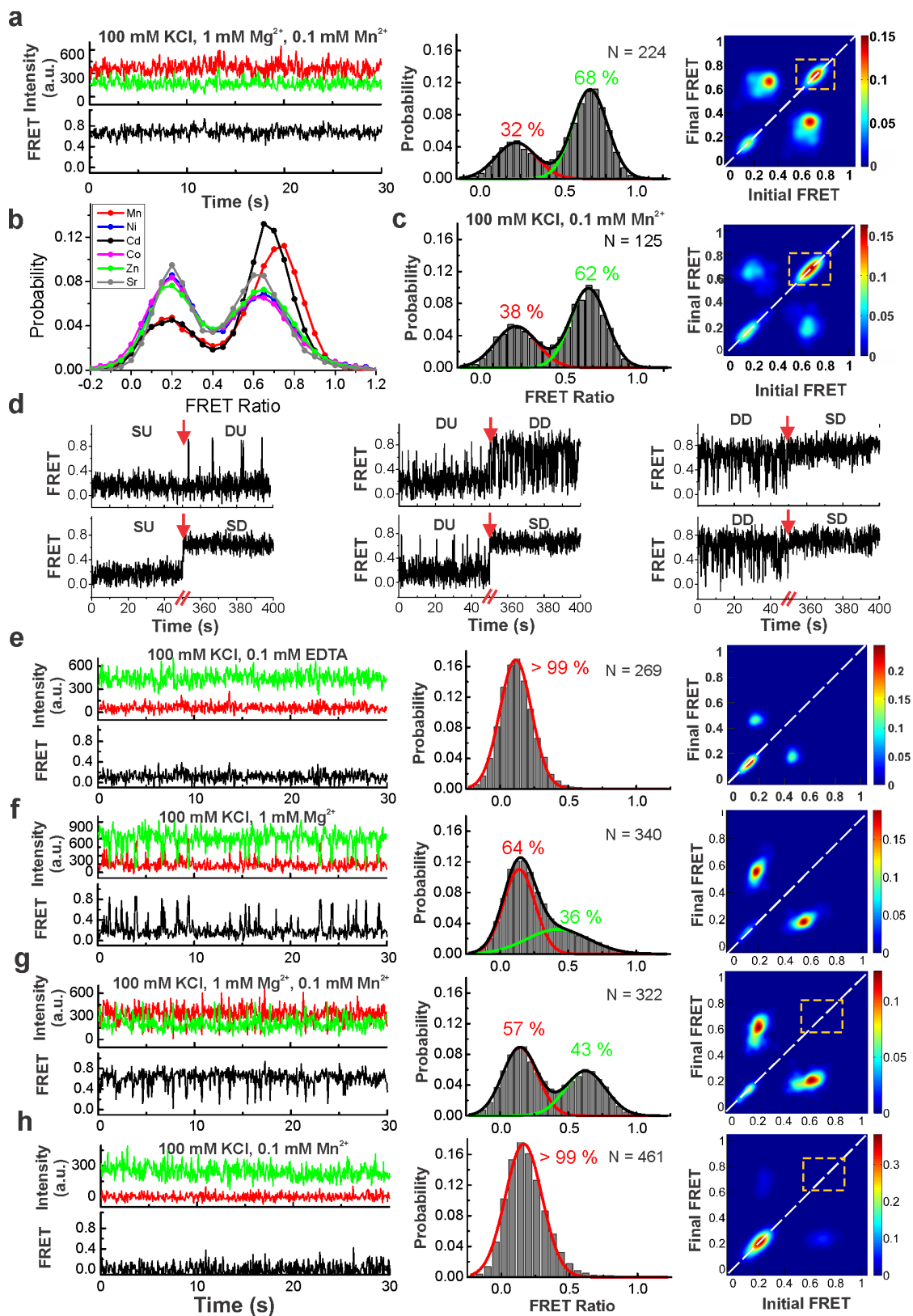


**Figure 5| Effect of  $Mn^{2+}$  and A48U mutation on the folding of the riboswitch.** (a) Representative smFRET trace, FRET histogram and TODP for the WT riboswitch in the presence of 0.1 mM  $Mn^{2+}$  and 1 mM  $Mg^{2+}$ . The stable ‘static’ docked (SD) conformation appears only in the presence of  $Mn^{2+}$ , as highlighted by the dashed yellow box in the TODP. (b) FRET histograms for the WT riboswitch at 0.1 mM concentration of different transition metals in the presence of 1 mM  $Mg^{2+}$ . Over 150 molecules were analyzed for each histogram. The corresponding TODPs are shown in **Supplementary Fig. 16**. (c) FRET histogram and TODP with SD population highlighted by dashed yellow box for the WT riboswitch in the presence of 0.1 mM  $Mn^{2+}$  alone. (d) Example smFRET traces for the WT riboswitch showing transitions between SU, DU, DD and SD traces upon addition of 0.1 mM  $Mn^{2+}$ . Representative smFRET traces, FRET histograms and TODPs for the A48U mutant riboswitch under: (e) no divalents (+0.1 mM EDTA), (f) 1 mM  $Mg^{2+}$  alone, (g) 1 mM  $Mg^{2+}$  and 0.1 mM  $Mn^{2+}$ , and (h) 0.1 mM  $Mn^{2+}$  alone. The dashed yellow box highlights the absence of SD conformations for the A48U riboswitch in the presence of  $Mn^{2+}$ , in contrast to the WT riboswitch.

## Suddala, Price *et al.*, Figure 6

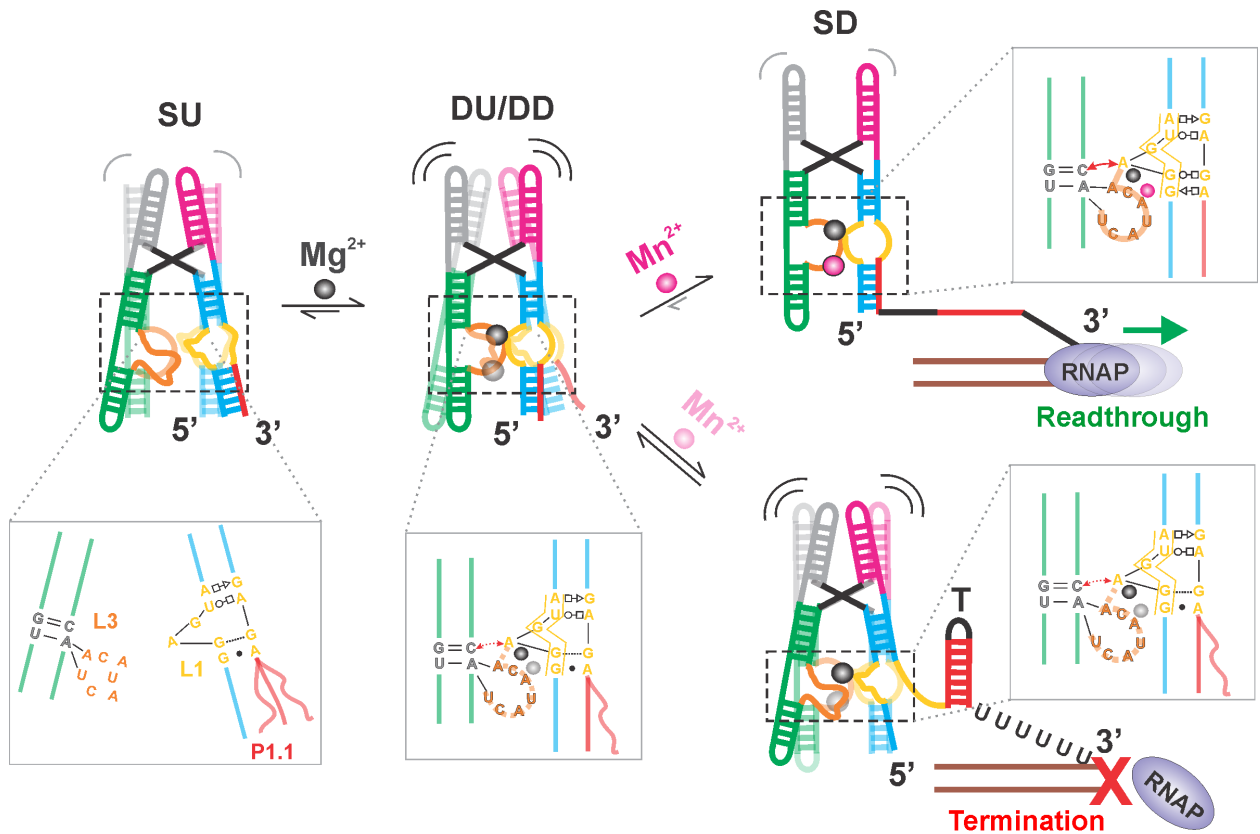


**Figure 6| Local-to-global signal transduction pathway in the core of the *Xory*  $\text{Mn}^{2+}$  sensing riboswitch.** The *Xory* riboswitch exists in an ‘X-shaped’ extended SU conformation in the absence of  $\text{Mg}^{2+}$ , with very rare transitions into docked ‘H-shaped’ conformations. In the SU state, the legs are far apart in the absence of a stable A-minor tertiary interaction and loops L3 and L1 are less structured under these conditions. In the presence of physiological  $\text{Mg}^{2+}$  concentrations (mM), the riboswitch samples docked conformations with distinct kinetics, indicative of differences in L3 stacking as observed in our crystal structures. L1 adopts an S-turn conformation (as indicated by the yellow box in the inset) and L3 is partially stacked under these conditions, aided by the presence of  $\text{Mg}^{2+}$  ions in  $M_{A,\text{Mg}}$  and transiently in  $M_{B,\text{Mn}}$ . In the presence of sufficient  $\text{Mn}^{2+}$ , binding of the metal ion by A48 reinforces L3 stacking and stability of the A-minor interaction. This maintains L1 in a rigid non-canonical SRL-like conformation that enables co-axial stacking



between P1.2 and the switch helix P1.1. In turn, this cascade of interactions stabilizes P1.1, thereby preventing strand invasion to favor formation of the antiterminator required for transcriptional read-through.

## ONLINE METHODS

### RNA preparation and crystallization

RNA was cloned, transcribed, purified, refolded with 2.5 mM  $\text{Mn}^{2+}$ , and screened for crystallization as previously described<sup>12</sup>. The *X. oryzae* aptamer domain sequence was modified to improve the chances of crystallization, including replacing the terminal loops in variable regions with GAAA tetraloops and adding a GG at the beginning of the sequence to increase T7 RNA polymerase efficiency<sup>36</sup>. We also removed a single unconserved U flip-out near the base of P1.1. In this construct, a native CA dinucleotide at the four-way junction was omitted from the sequence (**Fig. 1a**), possibly aiding crystallization. Initial crystal hits were obtained using the Nucleic Acid Mini-Screen (Hampton Research). This RNA crystallized at 0.2 mM in 10% MPD, 40 mM Na cacodylate (pH 7), 12 mM spermine tetrahydrochloride, 80 mM  $\text{SrCl}_2$ , and 20 mM  $\text{MgCl}_2$  after 2-3 months at 18 °C.

### X-ray data collection and structure building

A 2.85 Å resolution X-ray diffraction dataset was collected at NE-CAT beamline 24-ID-C at the Advanced Photon Source (Argonne, IL), at 0.769 Å wavelength in order to use the Strontium K-edge for phasing. An additional dataset was collected at a remote wavelength (0.7749 Å) for SIRAS. Datasets were processed by XDS<sup>37</sup> as part of NE-CAT's RAPD pipeline. An initial solution was achieved by molecular replacement using the central region of the *L. lactis* structure<sup>12</sup> followed by finding portions of external helices<sup>38</sup>. This partial solution was then used for MR-SAD in AutoSol in the Phenix suite<sup>39,40</sup> to find Sr sites and obtain an initial electron density map. Since this dataset was collected near the Sr K-edge wavelength (0.769 Å), we could observe anomalous signal from  $\text{Sr}^{2+}$  ions in the crystal. At 4  $\sigma$  (a relatively low threshold), there was modest signal at the Conformer 2  $\text{M}_{\text{A,Mg}}$  site, suggesting only partial occupancy by  $\text{Sr}^{2+}$  (**Fig. 2b**). However, there is no occupancy seen at any of the other  $\text{M}_{\text{A,Mg}}$  or  $\text{M}_{\text{B,Mn}}$  sites, despite there being external sites in the lattice with stronger anomalous signal (**Supplementary Fig. 1**). This suggests that the Conformer 2  $\text{M}_{\text{B,Mn}}$  site, despite lacking several contacts, can still distinguish between metals. It possibly discriminates by geometry; the  $\text{Sr}^{2+}$  ionic radius is 2.4 Å, compared to the smaller  $\text{Mn}^{2+}$  (2.2 Å) or  $\text{Mg}^{2+}$  (2.1 Å).  $\text{Mg}^{2+}$  cannot be differentiated from  $\text{Mn}^{2+}$  at the wavelength and resolution of this structure. Alternating rounds of building in Coot<sup>41</sup> and refinement with phenix.refine<sup>42</sup> and intermittent re-phasing and density modification in AutoSol were used to build the final model (**Supplementary Table 1**).

## Molecular Dynamics Simulations

The crystal structures of  $\text{Mn}^{2+}$  sensing riboswitch from *X. oryzae* from this study (both Conformers 1 and 2) and from *L. lactis* (PDB ID 4Y1I<sup>12</sup>) were used as starting structures for MD simulations. We aimed to study the effect of divalents in the metal ion binding sites on the structural dynamics of the riboswitch, so we prepared a set of starting structures containing different ions ( $\text{Mn}^{2+}$ ,  $\text{Mg}^{2+}$ , and  $\text{K}^+$ ) in the  $\text{M}_{\text{A,Mg}}$  and  $\text{M}_{\text{B,Mn}}$  sites (**Table 1**). In addition, we probed both for syn- and anti-conformations of A48 in Conformer 2 from *Xory* to verify refinement of the corresponding electron density as a *syn*-oriented nucleotide. Starting structures of the SRL-like motif lacking tertiary interactions with the rest of the aptamer were prepared from the crystal structures but entailing only the P1.1, P1.2 and L1 segments without divalents.

**Table 1.** Complete list of our 29 MD simulations of distinct start conditions and lengths, comprising a cumulative 53  $\mu\text{s}$  simulation time

Organism	PDB ID	Structure	Chain	Ions in active site		solvent box	Length
				$\text{M}_{\text{A,Mg}}$	$\text{M}_{\text{B,Mn}}$		
<i>L. lactis</i>	4Y1I	complete	A	$\text{Mg}^{2+}$	$\text{Mn}^{2+}$	rectangular	Each 3 $\mu\text{s}$
				$\text{Mg}^{2+}$	$\text{K}^+$		
				$\text{K}^+$	$\text{Mn}^{2+}$		
				$\text{K}^+$	$\text{K}^+$		
		P1.2 L1 P1.1	A	-	-	rectangular	3 $\mu\text{s}$
<i>X. oryzae</i>	This study	complete	Conformer 2 with <i>anti</i> A48	$\text{Mg}^{2+}$	$\text{Mn}^{2+}$	octahedral	Each 2 $\mu\text{s}$
				$\text{Mg}^{2+}$	$\text{K}^+$		
				$\text{K}^+$	$\text{Mn}^{2+}$		
				$\text{K}^+$	$\text{K}^+$		
			Conformer 2 with <i>syn</i> A48	$\text{Mg}^{2+}$	$\text{Mn}^{2+}$		
				$\text{Mg}^{2+}$	$\text{K}^+$		
				$\text{K}^+$	$\text{Mn}^{2+}$		
				$\text{K}^+$	$\text{K}^+$		
		P1.2 L1 P1.1	Conformer 2	-	-	rectangular	3 $\mu\text{s}$
		complete	Conformer 1	$\text{Mg}^{2+}$	$\text{Mn}^{2+}$	octahedral	Each twice 2 $\mu\text{s}$
				$\text{Mg}^{2+}$	$\text{K}^+$		
				$\text{K}^+$	$\text{Mn}^{2+}$		
				$\text{K}^+$	$\text{K}^+$		
		P1.2 L1 P1.1	Conformer 1	-	-	rectangular	3 $\mu\text{s}$

All MD simulations were carried out using pmemd.cuda (GPU code of AMBER 14 program package)<sup>43,44</sup> with the ff99bsc0 $\chi_{\text{OL3}}$  force field<sup>45-47</sup>. The simulation protocol was as follows. The structure with the RNA molecule and any ions in the  $\text{M}_{\text{A,Mg}}$  and  $\text{M}_{\text{B,Mn}}$  sites was immersed into a solvation box of SPC/E explicit water molecules<sup>48</sup>. We added KCl salt excess corresponding to

150 mM KCl. We used following ionic parameters:  $K^+$  ( $r = 1.593 \text{ \AA}$ ,  $\epsilon = 0.4297 \text{ kcal/mol}^{49}$ ),  $Mg^{2+}$  ( $r = 1.5545 \text{ \AA}$ ,  $\epsilon = 0.00295 \text{ kcal/mol}^{50}$ ),  $Mn^{2+}$  ( $r = 1.4060 \text{ \AA}$ ,  $\epsilon = 0.0167 \text{ kcal/mol}^{51}$ ), and  $Cl^-$  ( $r = 2.711 \text{ \AA}$ ,  $\epsilon = 0.0127 \text{ kcal/mol}^{49}$ ). Where indicated, we replaced one or both divalent ions in the  $M_{A,Mg}$  and  $M_{B,Mn}$  sites by  $K^+$  monovalents so that we probed for each specific starting structure four different ionic configurations in these ion binding sites (**Supplementary Table 2**). The solvated systems were equilibrated as follows. Geometrical optimization of hydrogen atoms was followed by optimization of waters and ions, while the position of the RNA molecule remained restrained. Subsequently, all RNA atoms were restrained and the solvent molecules with counter-ions were allowed to move during a 500-ps long MD run under NpT conditions ( $p = 1 \text{ atm}$ ,  $T = 298.16 \text{ K}$ ) to relax the total density of solvent surrounding the RNA. Next, the RNA molecule was relaxed by several minimization runs, with decreasing force constant of position restraints applied to the sugar-phosphate backbone. After full relaxation, the system was heated in two steps: The first step involved heating under NVT conditions for 100 ps, whereas the second step involved final density equilibration under NpT conditions for an additional 100 ps. The particle-mesh Ewald (PME) method for treating electrostatic interactions was used, and simulation were performed under periodic boundary conditions in the [NVT] ensemble at 298.16 K using a weak coupling Berendsen thermostat with a coupling time of 0.2 ps. The SHAKE algorithm, with a tolerance of  $10^{-5} \text{ \AA}$ , was used to fix the positions of all hydrogen atoms, and a 10.0  $\text{\AA}$  cut-off was applied to non-bonding interactions. The hydrogen mass repartitioning was used to change the mass of hydrogen and neighboring atoms to allow a 4 fs integration step. In the production runs of the isolated SRL-like motif (P1.2, L1, and P1.1 segments only) we applied upper-wall positional restraints to the hydrogen bonds of the terminal base pair of the P1.2 stem (i.e., the G16=C89 base pair proximal to the P2 stem in the complete structure) to mimic the stabilization effect of coaxial stacking of this base pair on the P2 stem. A parabolic restraint potential was applied at heavy atom distances of the particular hydrogen bonds above 3.5  $\text{\AA}$  with a force constant of  $2.5 \text{ kcal/mol/\AA}^2$ . The simulation time for each studied system was at least 2  $\mu\text{s}$  (**Supplementary Table 2**).

## Data analysis

All trajectories were analyzed with the Ptraj module of the AMBER package<sup>44</sup> and the simulations were visualized using VMD<sup>52</sup>. B-factors were calculated as average mass-weighted fluctuation of each residue over the entire trajectory aligned to the stem closest to the residue. This guarantees that the B-factors are not influenced by global motions and reflect local flexibilities only. The

stacking interactions were detected using the G-vector of an eRMSD metric and were annotated using baRNAb<sup>53</sup>.

### **Single-molecule FRET RNA preparation**

The RNA for smFRET studies was annealed from two synthetic RNA oligonucleotides (**Supplementary Fig. 13**), ordered with the indicated modifications from IDT. The native CA dinucleotide omitted for crystallization was present in the smFRET RNA. Oligonucleotide 1 has a 5'-Cy5 and oligonucleotide 2 has 5'-Cy3 and 3' biotin-TEG. In this two oligonucleotide design of the smFRET construct, the donor fluorophore Cy3 and biotin-TEG were placed on the 5' and 3' ends of stem P1.1 while the acceptor fluorophore Cy5 is attached to the 5' end of P3.2, positioning the fluorophores on either end of the distal arms that dock. For specifically probing the docking interaction, we extended the stem P1.1 to prevent end fraying. The biotin on the 3'-end of P1.1 was used for immobilization of the RNA onto a microscope quartz slide and subsequent prism-based total internal reflection fluorescence microscopy (TIRFM, **Fig. 4a**). Optimal refolding of the RNA was achieved with a mixture of 1  $\mu$ M oligonucleotide 1 and 1.5  $\mu$ M oligonucleotide 2 in 20 mM HEPES pH 7.0, 50 mM KCl. In PCR tubes, samples were heated to 70 °C for 2 min, then 2 mM MgCl<sub>2</sub> was added, samples were allowed to cool to RT for 10 min, then put on ice until further use. To check assembly, ~1 pmol of each oligonucleotide (1-2  $\mu$ L) was added to 10  $\mu$ L running buffer supplemented with 10% glycerol and loaded onto a non-denaturing 8% polyacrylamide gel run at 4 °C. A buffer of 0.5x TBE supplemented with 2 mM Mg(OAc)<sub>2</sub> and 50 mM KCl was used in the gel and as the running buffer.

### **smFRET data acquisition and analysis**

A small microfluidic channel was made by sandwiching a cleaned quartz slide and a glass coverslip using double-side tape. Beforehand, two holes were drilled into the quartz slide and afterwards tubing was attached to them to act as inlet and outlet ports that were used for flowing buffer and introducing the RNA. The two RNA oligonucleotides containing the Cy3, Cy5 and biotin modifications were mixed at a concentration of 2  $\mu$ M each in 50 mM Hepes, pH 7.2, 100 mM KCl (1x buffer). The RNA was heated at 90 °C for 2 min, left at RT for 30 s to cool down, followed by addition of 2 mM MgCl<sub>2</sub> and slow cooling down to RT over 15 min. This annealed RNA stock was used for carrying out smFRET experiments, for which a 15-25 pM RNA solution was made by diluting the 2  $\mu$ M annealed stock using 1x buffer.

100  $\mu$ L of diluted RNA solution was flowed onto the quartz slide coated with biotinylated-BSA and streptavidin for immobilization and incubated for 2 min. Any unbound RNA was washed off using 1x buffer. This step also washes off small (low nM) amounts of residual  $Mg^{2+}$  present in the stock. For experiments in the absence of divalents, 0.1 mM EDTA was included in the 1x buffer to chelate any contaminating divalent ions.  $Mg^{2+}$  titration experiments were performed on the same slide after washing off the EDTA using 1x buffer. We included an enzymatic oxygen scavenging system (OSS) containing 50 nM protocatechuate-3,4-dioxygenase and 5 mM protocatechuic acid in 1x buffer to prolong the longevity of the fluorophores. In addition, 2 mM Trolox (6-Hydroxy-2,5,7,8-tetramethylchromane-2-carboxylic acid) was included in the imaging buffer to suppress photoblinking of the dyes.

All smFRET movies were acquired at  $\sim 16$  Hz, unless otherwise specified, using a prism-based total internal reflection fluorescence (TIRF) microscope with an intensified CCD (IPentamax, Princeton Instruments) or sCMOS camera (Hamamatsu ORCA-Flash4.0 V3), essentially as previously described<sup>54,55</sup>. Cy3 on the RNA was excited using a 532 nm laser and the emission from both Cy3 (donor) and Cy5 (acceptor) were simultaneously detected side-by-side on the camera. Towards the end of all movies, the Cy5 was directly excited using a 640 nm laser to check for the presence of the acceptor (Cy5) fluorophore. This helps in distinguishing the low-FRET ( $\sim 0.1$  FRET) states we observe from  $\sim 0$  FRET states due to the absence or photobleaching of Cy5 in Cy3-labeled molecules. Raw movies were analyzed using IDL (Research Systems) to extract the time traces for all spots in Cy3 and Cy5 channels. Single molecule traces were then visualized using Matlab and only those with a minimum combined intensity (Cy3 + Cy5 intensity) of 300, showing single-step photobleaching of the dyes, a signal-to-noise ratio of  $>3$ , and longer than 6 s were selected for further analysis. Selected traces were then background-subtracted to correct for cross-talk and (minimal) bleed-through. We calculated the FRET ratio as  $I_A/(I_A+I_D)$ , where  $I_A$  and  $I_D$  are the background corrected intensities of acceptor (Cy5) and donor (Cy3), respectively. FRET histograms were made using the first 50 frames (3 s) of all traces (at least 200) in a given condition and fit with a sum of Gaussians using OriginPro 8.5. For kinetic analysis, traces were idealized with a two-state model corresponding to undocked (low-FRET) and docked (high-FRET) states using the segmental k-means algorithm in QuB software as previously described<sup>56,57</sup>. Cumulative dwell-time histograms were plotted from all extracted dwell times and fit with single- or double-exponential functions using OriginPro 8.5 to obtain the lifetimes in the

undocked ( $\tau_{\text{undock}}$ ) and docked ( $\tau_{\text{dock}}$ ) states. Rate constants of docking and undocking were then calculated as  $k_{\text{dock}} = 1/\tau_{\text{undock}}$  and  $k_{\text{undock}} = 1/\tau_{\text{dock}}$ . For the double-exponential fits, kinetics were calculated similarly using both the short and long dwell lifetimes to obtain the fast and slow rate constants, respectively.

## REFERENCES

1. Mandal, M. & Breaker, R.R. Gene regulation by riboswitches. *Nat. Rev. Mol. Cell Biol.* **5**, 451-63 (2004).
2. Serganov, A. & Nudler, E. A decade of riboswitches. *Cell* **152**, 17-24 (2013).
3. McCown, P.J., Corbino, K.A., Stav, S., Sherlock, M.E. & Breaker, R.R. Riboswitch diversity and distribution. *Rna* **23**, 995-1011 (2017).
4. Grundy, F.J. & Henkin, T.M. The S box regulon: a new global transcription termination control system for methionine and cysteine biosynthesis genes in Gram-positive bacteria. *Mol. Microbiol.* **30**, 737-749 (1998).
5. Winkler, W., Nahvi, A. & Breaker, R.R. Thiamine derivatives bind messenger RNAs directly to regulate bacterial gene expression. *Nature* **419**, 952-6 (2002).
6. Smith, K.D. et al. Structural basis of ligand binding by a c-di-GMP riboswitch. *Nat. Struct. Mol. Biol.* **16**, 1218-1223 (2009).
7. Nelson, J.W. et al. Riboswitches in eubacteria sense the second messenger c-di-AMP. *Nat. Chem. Biol.* **9**, 834-839 (2013).
8. Sudarsan, N. et al. Riboswitches in Eubacteria Sense the Second Messenger Cyclic Di-GMP. *Science* **321**, 411-413 (2008).
9. Green, N.J., Grundy, F.J. & Henkin, T.M. The T box mechanism: tRNA as a regulatory molecule. *FEBS Lett.* **584**, 318-24 (2010).
10. Dann, C.E., 3rd et al. Structure and mechanism of a metal-sensing regulatory RNA. *Cell* **130**, 878-92 (2007).
11. Wedekind, J.E., Dutta, D., Belashov, I.A. & Jenkins, J.L. Metalloriboswitches: RNA-based inorganic ion sensors that regulate genes. *J. Biol. Chem.* **292**, 9441-9450 (2017).
12. Price, I.R., Gaballa, A., Ding, F., Helmann, J.D. & Ke, A. Mn(2+)-sensing mechanisms of yybP-ykoY orphan riboswitches. *Mol. Cell* **57**, 1110-23 (2015).
13. Suddala, K.C. & Walter, N.G. Riboswitch structure and dynamics by smFRET microscopy. *Methods Enzymol.* **549**, 343-73 (2014).
14. Jones, C.P. & Ferre-D'Amare, A.R. Long-Range Interactions in Riboswitch Control of Gene Expression. *Annu Rev Biophys* **46**, 455-481 (2017).
15. Barrick, J.C.K., Winkler WC, Nahvi A, Mandal M, Collins J, Lee M, Roth A, Sudarsan N, Jona I, Wickiser JK, Breaker RR New RNA motifs suggest an expanded scope for riboswitches in bacterial genetic control. *Proc. Natl. Acad. Sci. USA* **101**, 6421-6426 (2004).
16. Argaman, L. et al. Novel small RNA-encoding genes in the intergenic regions of Escherichia coli. *Curr. Biol.* **11**, 941-50 (2001).
17. Breaker, R.R. Riboswitches and the RNA world. *Cold Spring Harb. Perspect. Biol.* **4**(2012).
18. Dambach, M. et al. The ubiquitous yybP-ykoY riboswitch is a manganese-responsive regulatory element. *Mol. Cell* **57**, 1099-109 (2015).
19. Liang, H. et al. Identification and functional characterization of small non-coding RNAs in Xanthomonas oryzae pathovar oryzae. *BMC Genomics* **12**, 87 (2011).

20. Li, C.T., J; Mao, D; He, C. A novel manganese efflux system, YebN, is required for virulence by *Xanthomonas oryzae* pv. *oryzae*. *PLoS One* **6**, e21983 (2011).
21. Leontis, N.B., Stombaugh, J. & Westhof, E. The non-Watson-Crick base pairs and their associated isostericity matrices. *Nucleic Acids Res.* **30**, 3497-531 (2002).
22. Spomer, J. et al. RNA Structural Dynamics As Captured by Molecular Simulations: A Comprehensive Overview. *Chem. Rev.* **118**, 4177-4338 (2018).
23. Ditzler, M.A., Otyepka, M., Spomer, J. & Walter, N.G. Molecular dynamics and quantum mechanics of RNA: conformational and chemical change we can believe in. *Acc. Chem. Res.* **43**, 40-7 (2010).
24. Duarte, C.M., Wadley, L.M. & Pyle, A.M. RNA structure comparison, motif search and discovery using a reduced representation of RNA conformational space. *Nucleic Acids Res.* **31**, 4755-61 (2003).
25. Zhuang, X. et al. Correlating structural dynamics and function in single ribozyme molecules. *Science* **296**, 1473-6 (2002).
26. Rueda, D. et al. Single-molecule enzymology of RNA: essential functional groups impact catalysis from a distance. *Proceedings of the National Academy of Sciences of the United States of America* **101**, 10066-71 (2004).
27. Okumus, B., Wilson, T.J., Lilley, D.M. & Ha, T. Vesicle encapsulation studies reveal that single molecule ribozyme heterogeneities are intrinsic. *Biophysical journal* **87**, 2798-806 (2004).
28. Ditzler, M.A., Rueda, D., Mo, J., Hakansson, K. & Walter, N.G. A rugged free energy landscape separates multiple functional RNA folds throughout denaturation. *Nucleic acids research* **36**, 7088-99 (2008).
29. Fiore, J.L., Kraemer, B., Koberling, F., Edmann, R. & Nesbitt, D.J. Enthalpy-driven RNA folding: single-molecule thermodynamics of tetraloop-receptor tertiary interaction. *Biochemistry* **48**, 2550-8 (2009).
30. Greenfeld, M., Solomatin, S.V. & Herschlag, D. Removal of covalent heterogeneity reveals simple folding behavior for P4-P6 RNA. *The Journal of biological chemistry* **286**, 19872-9 (2011).
31. Solomatin, S.V., Greenfeld, M. & Herschlag, D. Implications of molecular heterogeneity for the cooperativity of biological macromolecules. *Nature structural & molecular biology* **18**, 732-4 (2011).
32. Solomatin, S.V., Greenfeld, M., Chu, S. & Herschlag, D. Multiple native states reveal persistent ruggedness of an RNA folding landscape. *Nature* **463**, 681-4 (2010).
33. Marek, M.S., Johnson-Buck, A. & Walter, N.G. The shape-shifting quasispecies of RNA: one sequence, many functional folds. *Physical chemistry chemical physics : PCCP* **13**, 11524-37 (2011).
34. Furukawa, K. et al. Bacterial riboswitches cooperatively bind Ni(2+) or Co(2+) ions and control expression of heavy metal transporters. *Mol. Cell* **57**, 1088-98 (2015).
35. Wakeman, C.A., Ramesh, A. & Winkler, W.C. Multiple metal-binding cores are required for metalloregulation by M-box riboswitch RNAs. *Journal of molecular biology* **392**, 723-35 (2009).
36. Pleiss, J.A.D., M. L.; Uhlenbeck, O. C. T7 RNA polymerase produces 5' end heterogeneity during in vitro transcription from certain templates. *RNA* **4**, 1313-7 (1988).
37. Kabsch, W. XDS. *Acta Cryst.* **D66**, 125-132 (2010).
38. Robertson, M.P., Chi, Y.-I. & Scott, W.G. Solving novel RNA structures using only secondary structural fragments. *Methods* **52**, 168-172 (2010).
39. Adams, P.D. et al. PHENIX: a comprehensive Python-based system for macromolecular structure solution. *Acta Crystallogr. D Biol. Crystallogr.* **66**, 213-21 (2010).
40. Terwilliger, T.C. et al. Decision-making in structure solution using Bayesian estimates of map quality: the PHENIX AutoSol wizard. *Acta Crystallogr. D Biol. Crystallogr.* **65**, 582-601 (2009).
41. Emsley, P., Lohkamp, B., Scott, W.G. & Cowtan, K. Features and development of Coot. *Acta Crystallogr. D Biol. Crystallogr.* **66**, 486-501 (2010).



42. Afonine, P.V. et al. Towards automated crystallographic structure refinement with phenix.refine. *Acta Crystallogr. D Biol. Crystallogr.* **68**, 352-67 (2012).
43. Salomon-Ferrer, R., Gotz, A.W., Poole, D., Le Grand, S. & Walker, R.C. Routine Microsecond Molecular Dynamics Simulations with AMBER on GPUs. 2. Explicit Solvent Particle Mesh Ewald. *J. Chem. Theory Comput.* **9**, 3878-88 (2013).
44. Case, D.A. et al. *AMBER 2016*, (University of California San Francisco, San Francisco, 2016).
45. Banáš, P. et al. Performance of Molecular Mechanics Force Fields for RNA Simulations: Stability of UUCG and GNRA Hairpins. *Journal of Chemical Theory and Computation* **6**, 3836-3849 (2010).
46. Perez, A. et al. Refinement of the AMBER force field for nucleic acids: improving the description of alpha/gamma conformers. *Biophys. J.* **92**, 3817-29 (2007).
47. Zgarbova, M. et al. Refinement of the Cornell et al. Nucleic Acids Force Field Based on Reference Quantum Chemical Calculations of Glycosidic Torsion Profiles. *J. Chem. Theory Comput.* **7**, 2886-2902 (2011).
48. Berendsen, H.J.C., Grigera, J.R. & Straatsma, T.P. The missing term in effective pair potentials. *The Journal of Physical Chemistry* **91**, 6269-6271 (1987).
49. Joung, I.S. & Cheatham, T.E., 3rd. Determination of alkali and halide monovalent ion parameters for use in explicitly solvated biomolecular simulations. *J. Phys. Chem. B* **112**, 9020-41 (2008).
50. Allnér, O., Nilsson, L. & Villa, A. Magnesium Ion–Water Coordination and Exchange in Biomolecular Simulations. *Journal of Chemical Theory and Computation* **8**, 1493-1502 (2012).
51. Li, P., Roberts, B.P., Chakravorty, D.K. & Merz, K.M. Rational Design of Particle Mesh Ewald Compatible Lennard-Jones Parameters for +2 Metal Cations in Explicit Solvent. *J. Chem. Theory Comput.* **9**, 2733-2748 (2013).
52. Humphrey, W., Dalke, A. & Schulten, K. VMD: visual molecular dynamics. *J. Mol. Graph.* **14**, 33-8, 27-8 (1996).
53. Bottaro, S., Di Palma, F. & Bussi, G. The role of nucleobase interactions in RNA structure and dynamics. *Nucleic Acids Res.* **42**, 13306-14 (2014).
54. Michelotti, N., de Silva, C., Johnson-Buck, A.E., Manzo, A.J. & Walter, N.G. A bird's eye view tracking slow nanometer-scale movements of single molecular nano-assemblies. *Methods Enzymol.* **475**, 121-48 (2010).
55. Juetten, M.F. et al. Single-molecule imaging of non-equilibrium molecular ensembles on the millisecond timescale. *Nat. Methods* **13**, 341-4 (2016).
56. Qin, F. & Li, L. Model-based fitting of single-channel dwell-time distributions. *Biophys. J.* **87**, 1657-71 (2004).
57. Blanco, M. & Walter, N.G. Analysis of complex single-molecule FRET time trajectories. *Methods Enzymol.* **472**, 153-78 (2010).

## **Supplementary Information**

# **Local-to-global signal transduction at the core of the Mn<sup>2+</sup> sensing riboswitch**

**Krishna C. Suddala<sup>1\*</sup>, Ian R. Price<sup>2\*</sup>, Michal Janeček<sup>3</sup>, Petra Kührová<sup>4</sup>, Shiba Dandpat<sup>1</sup>, Jiří Šponer<sup>3,4</sup>,  
Pavel Banáš<sup>3,4</sup>, Ailong Ke<sup>2</sup>, Nils G. Walter<sup>1</sup>**

<sup>1</sup>Single Molecule Analysis Group and Center for RNA Biomedicine, Department of Chemistry, University of Michigan, Ann Arbor, MI, 48105,

<sup>2</sup>Department of Molecular Biology and Genetics, Cornell University, Ithaca, NY 14850

<sup>3</sup>Institute of Biophysics of the Czech Academy of Sciences, Kralovopolská 135, 612 65 Brno, Czech Republic

<sup>4</sup>Regional Centre of Advanced Technologies and Materials, Department of Physical Chemistry, Faculty of Science, Palacký University, tř. 17 listopadu 12, 771 46, Olomouc, Czech Republic

**Table S1**

	<b><u>X. oryzae-Mn<sup>2+</sup></u></b>
Beamline	APS 24 ID-C
Wavelength (Å)	0.7690
Resolution range (Å)	62.64-2.85 (2.95-2.85)
Space group	P 21 21 21
Unit cell	81.30 85.17 92.46 90.00° 90.00° 90.00°
Total reflections	119014 (11355)
Unique reflections	15512 (1510)
Multiplicity	7.7 (7.6)
Completeness (%)	99.8 (99.1)
Mean I/sigma(I)	12.9 (0.66)
Wilson B-factor	83.22
R-merge	0.118 (2.93)
R-meas	0.127 (3.15)
CC1/2	1.00 (0.306)
CC*	1 (0.685)
Reflections used in refinement	15515 (1499)
Reflections used for R-free	1264 (121)
R-work	0.209 (0.688)
R-free	0.221 (0.726)
Total non-hydrogen atoms	4342
macromolecules	4279
ligands	56
water	7
RMS(bonds)	0.015
RMS(angles)	0.49
Clashscore	4.01
Average B-factor	69.85
macromolecules	69.17
ligands	93.63
solvent	66.69

**Table S1. Crystallographic data and refinement statistics for the *X. oryzae* aptamer structure**  
Figures in parentheses indicate statistics for the highest resolution shell.

**Figure S1**

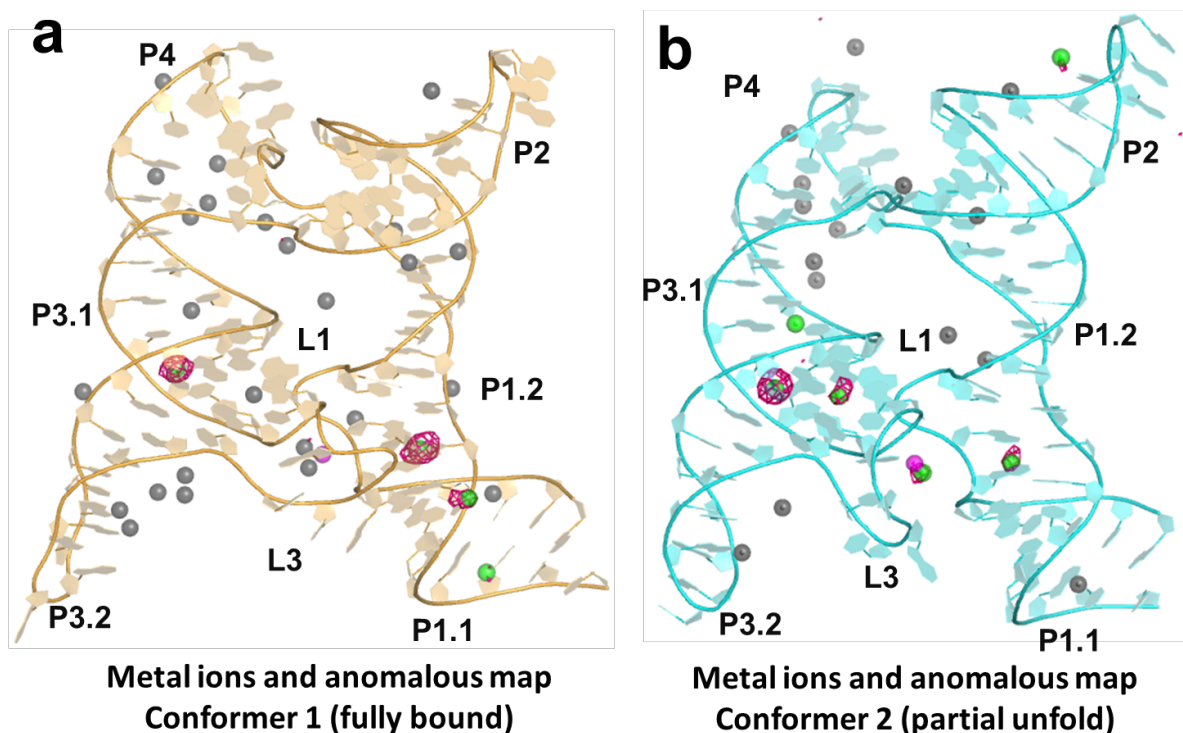


**Figure S1|. Overall ions and anomalous sites for the *X. oryzae* *yybP-ykoY* riboswitch crystal construct.** **a)** Conformer 1 (orange) and **b)** Conformer 2 (cyan). Total ions within 5 Å of A chain include 2  $\text{Mn}^{2+}$  (magenta), 45  $\text{Mg}^{2+}$  (or  $\text{Mn}^{2+}$ ) (black), and 9  $\text{Sr}^{2+}$  (green). The anomalous difference map, collected at 0.769 Å, is shown in pink mesh at level 4  $\sigma$ . Placement of  $\text{Sr}^{2+}$  ions was determined by anomalous map and/or high electron density. Since  $\text{Mn}^{2+}$  has minimal anomalous signal at this wavelength and it is similar in ionic radius to  $\text{Mg}^{2+}$ , it could not be differentiated from  $\text{Mg}^{2+}$ . Thus,  $\text{Mn}^{2+}$  (2.5 mM in the crystal) could partially or fully occupy sites denoted as  $\text{Mg}^{2+}$  (30 mM in the crystal). Binding site  $\text{Mn}^{2+}$  were predicted to be so based on previous analysis of the *L. lactis* structure, but were not confirmed by this structure.

**Figure S2**

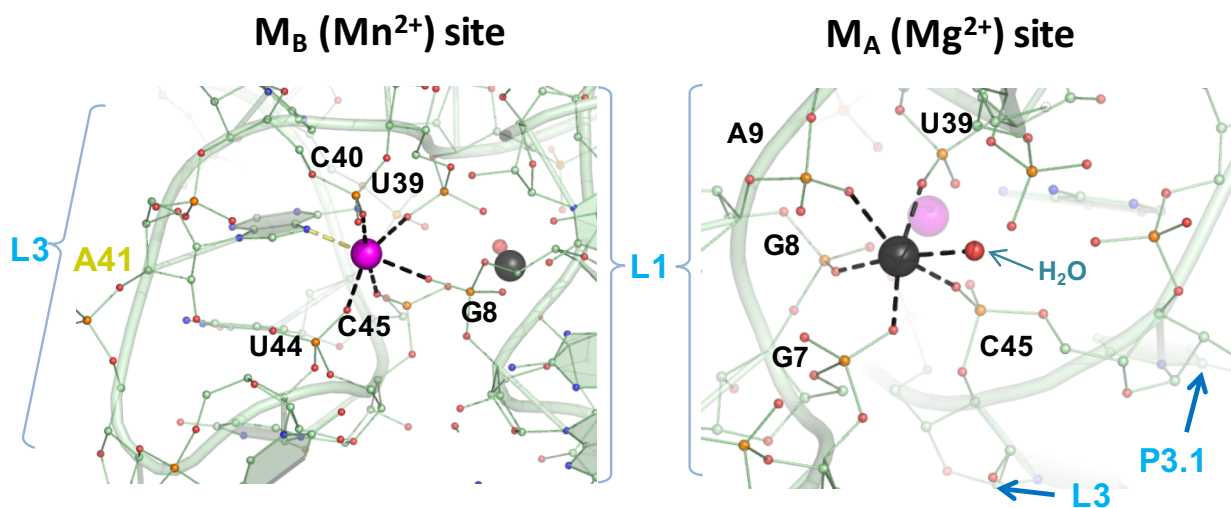


**Figure S2| Metal binding sites in the *L. lactis* yybP-ykoY structure.** Close-up view of the  $M_{B,Mn}$  (purple) and  $M_{A,Mg}$  (black) metal binding sites showing different contacts with surrounding L3 and L1 residues. The oxygen atoms of water molecules are shown as red spheres.

**Figure S3**

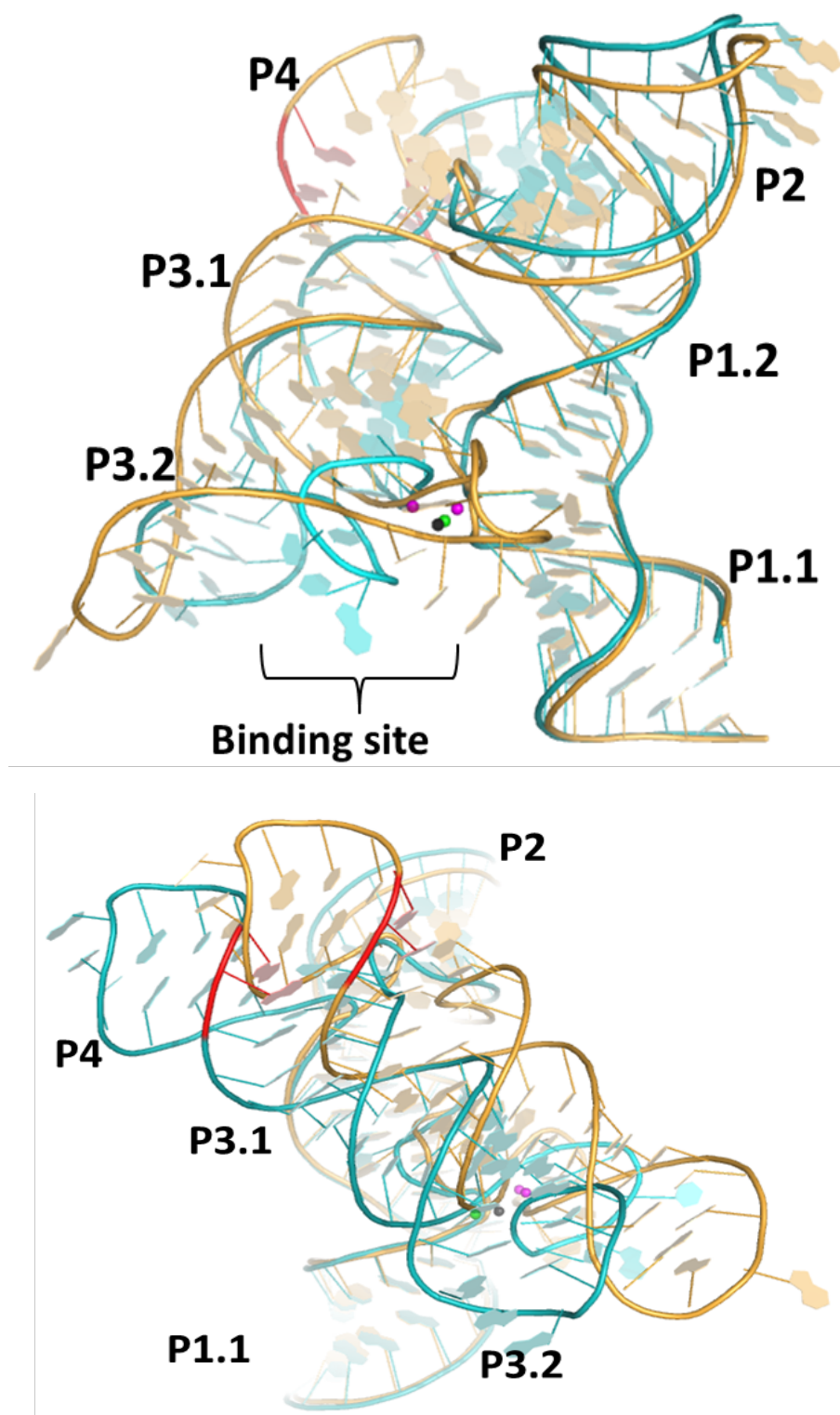


**Figure S3| Overall comparison of Conformers 1 and 2.** When aligned by L1, there is also a shift of the P3/P4 helical stack between Conformers 1 (orange) and 2 (cyan). The *L. lactis* structure (not shown) is intermediate but more similar to Conformer 1 when aligned in this way.

### Comparison of X-ray $Mn^{2+}$ bound structures to $Cd^{2+}$ bound structures

With respect to the recent finding that  $Cd^{2+}$  can also bind to the *yybP-ykoY* riboswitch<sup>1</sup>, our smFRET results and unpublished data from a *yybP-ykoY* and Broccoli-based fluorescent sensor agree with this conclusion. However, our structure (at 2.85 Å resolution) and previous ones with  $Mn^{2+}$  cannot provide strong evidence for or against their intriguing argument for heptacoordination as the mechanism of specificity for  $Mn^{2+}$ . While  $Cd^{2+}$  is heptacoordinate in their Llac-MntP structure (PDB ID 6CC3), with water as its seventh ligand, it is not clear how that water could enable a mechanism of specificity for  $Mn^{2+}$  against other metals. Further, in the highest-resolution structure (6CB3),  $Cd^{2+}$  at  $M_B$  was found to be hexacoordinate. The Llac-alx structure (6CC1) is also modelled as bound in a heptacoordinate fashion to  $M_B$ , with the seventh ligand here coming from a second phosphoryl oxygen from the same phosphate of U44. However, this structure is similar to all of our  $Mn^{2+}$ -bound structures, in that the resolution is not high enough to show the subtle difference in orientation of a phosphate that would be required to distinguish hexa- from hepta-coordination. As for the  $M_A$  site, our  $Cd^{2+}$ -only smFRET data suggest that  $M_A$  probably prefers either Mg or Mn over  $Cd^{2+}$ . Upon inspection of their data,  $M_A$  does not appear clearly heptacoordinate in any of their structures. It is actually octacoordinate in the Llac with Cd/Mg/Ba (PDB 6CB3) and another claim (Llac-MntP) relies on placed waters not seen in the electron density. A very high-resolution structure of a *yybP-ykoY* riboswitch with  $Mn^{2+}$  is required to address this interesting question. In any case, taken together with our structures, these agree with the finding of flexibility in the Mn-binding area, even when the riboswitch ligand is bound. It is a separate biological argument whether  $Cd^{2+}$  is a relevant ligand, as it in the past was often considered toxic and xenobiotic for most organisms, and its high-affinity binding to enzymes at sites of other metals is generally considered aberrant<sup>2</sup>.

### Global structural dynamics of docked structures of aptamers in the MD simulations

To elucidate structural dynamics of  $Mn^{2+}$  sensing riboswitch, we performed a set of explicit solvent MD simulations on microseconds time scale. In addition to simulations containing both  $M_A$  and  $M_B$  ion binding sites occupied by divalent ions, we performed a set of simulations testing the effect of replacement of these divalent ions by monovalents in each ion binding position separately or in both of them simultaneously (see **Table S2**).

The global structural dynamics of the studied systems was visualized by the B-factors calculated per residues (**Figure S4**). All simulations revealed similar trends in global structural dynamics except of behavior of L3 loop, which was found to be sensitive to type of ions in the  $M_A$  and  $M_B$  ion binding sites (see below). All stems exhibited high structural stability in all simulations. We observed larger fluctuations on the tips of P2, P3, and P4 stems. These fluctuations were found to be caused by unstacking of the L2 nucleotide, which should be considered as inherent part of native structural dynamics of GNRA tetraloops<sup>3-7</sup>. In the case of simulations of *L. lactis* structure, B-factor values indicated also large fluctuations of the P2 stem. Detailed analyses revealed that these fluctuations were connected with a reversible bending of the P2 stem and its movement toward and away from the P4 stem. This global movement was correlated with flipping of  $\epsilon$  torsion angle of A28 nucleotide, which fluctuated between two states (see **Figure S5**).

**Figure S4**

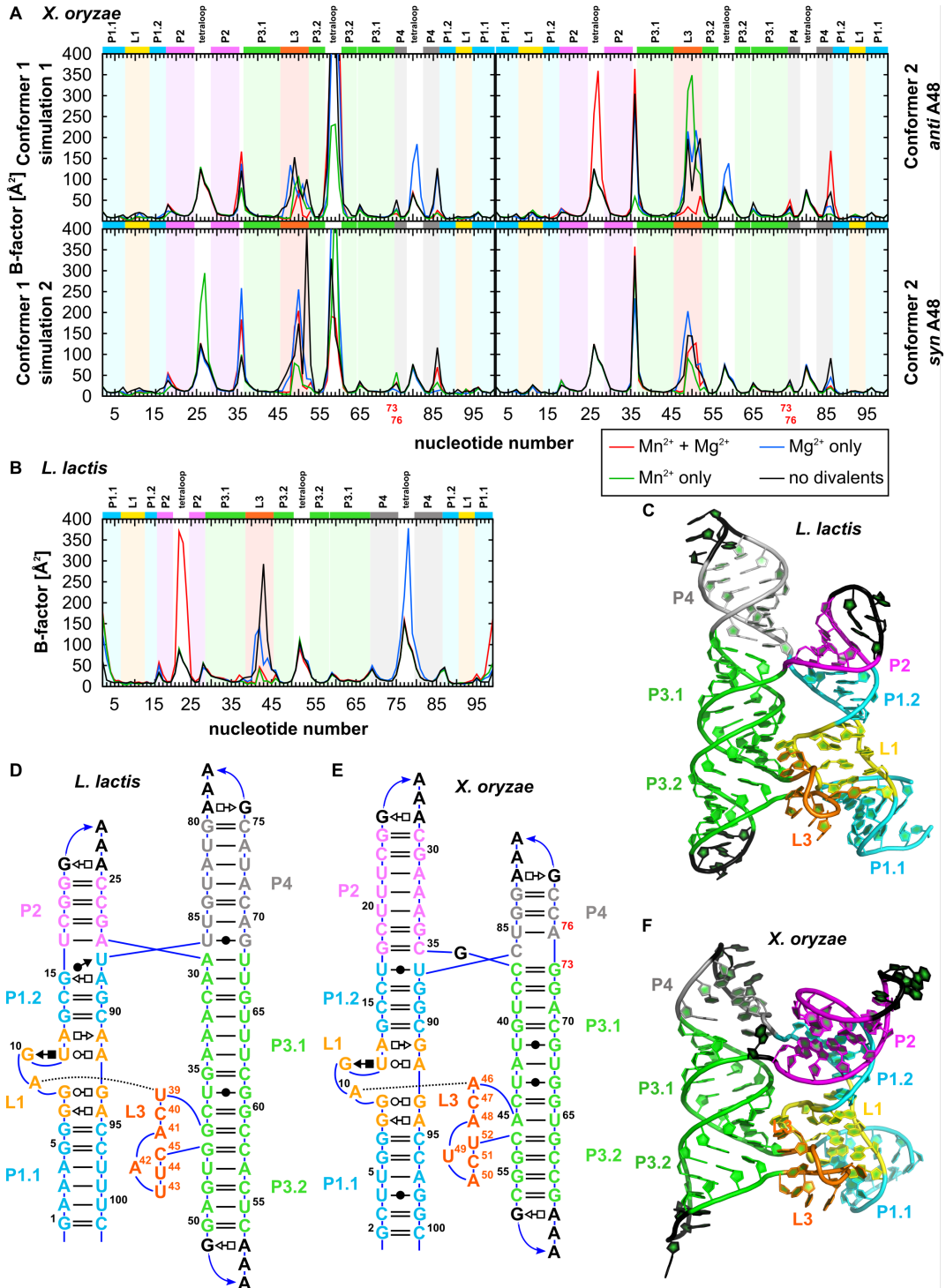


**Figure S4.** The average mass-weighted B-factor as a function of residue number obtained in MD simulations of Mn<sup>2+</sup> sensing riboswitch from A) *Xanthomonas oryzae* or B) *Lactococcus lactis* (see Table 1 in the main text for full list of the simulations). The colors of background bars correspond to the regions in the secondary and 3D structures shown on panels C-F.



**Figure S5**

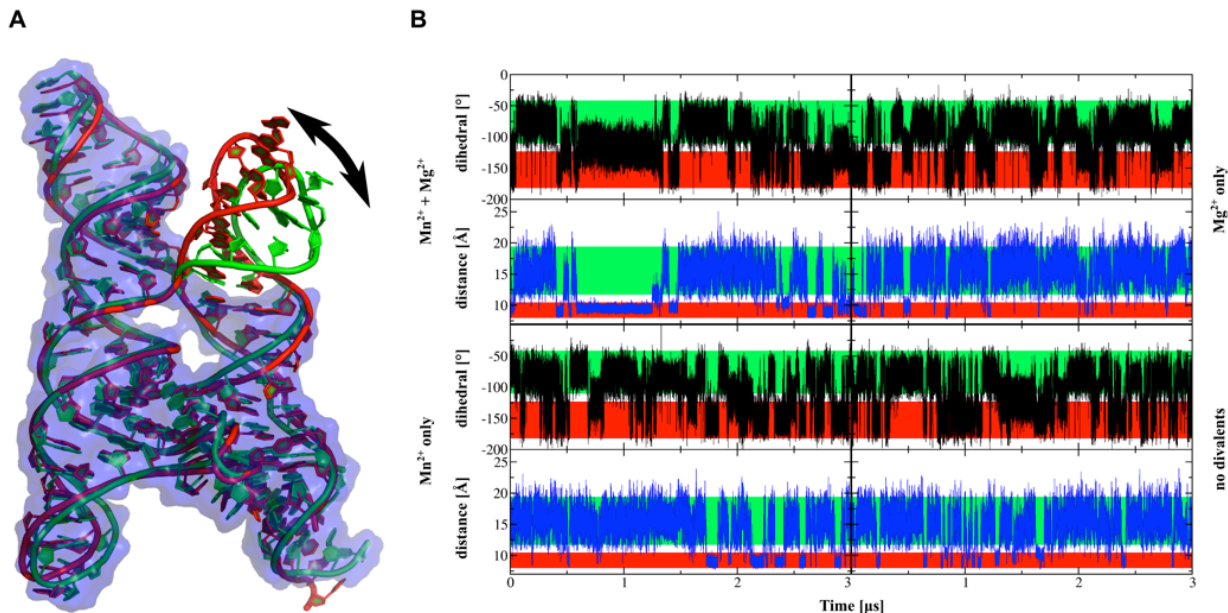


**Figure S5** | A) Superposition of the open and closed conformation (in green and red, respectively) observed in MD simulation of the aptamer from *L. lactis*. B) Time dependence of  $\epsilon$  dihedral angle of A28 (black line) and distance between P2 (center of mass of C17-G20 backbone) and P4 (center of mass of C71-A72 backbone) stems (blue line). The green and the red strips on the background correspond to the open (native crystal-like) and closed conformation, respectively.

## MD simulations confirmed *syn* orientation of A48 in L3 loop of *X. oryzae* structure

### Conformer 2

The electron density of the conformer 2 of the *X. oryzae* structure revealed adenine A48 in *syn*- rather than *anti*-conformation. In order to verify this unusual glycosidic bond orientation within the given structural context, we used two different refinements of the conformer 2 structure (**Figure S6**) as starting structures for subsequent MD simulations. These simulations aimed to indirectly probe the orientation of A48 glycosidic bond via analyses of compatibility of a given orientation of A48 with its structural environment reflecting the native A48 orientation through molecular interactions. We thus expected that while simulation starting from native orientation of A48 will fluctuate around starting structure conformation, the non-native orientation of A48 in the starting structure should result in structural changes in initial phase of MD simulation. For sake of completeness, it is also possible that both orientations of A48 might coexist in the crystal lattice ensemble and electron density represents ensemble-averaged picture of A48, which is structurally compatible with its structural environment in both orientations. In such case, both A48 orientations would be equally tolerated by their structural environment and thus both would be equally stable in MD simulations.

Therefore, we performed MD simulations of conformer 2 both with *syn*- and *anti*-oriented A48. Namely, we compared simulations having their ion binding sites occupied by corresponding native divalent ions, i.e., by  $Mg^{2+}$  and  $Mn^{2+}$  in  $M_A$  and  $M_B$ , respectively (see **Table S2**). We observed that the simulation started from structure with *syn*-oriented A48 stably fluctuated around crystal conformation during the entire 2  $\mu s$  simulation. In contrast, the simulation started with *anti*-oriented A48 revealed significant structural changes during initial phase of the simulation. Namely, the A48 nucleobase was shifted already in the initial geometrical optimization, so that it was coordinated to the  $Mn^{2+}$  ion by N7 nitrogen, while N6 exocyclic amino group was repelled away from the  $Mn^{2+}$  ion. This movement was accompanied by reconfiguration of the sugar-phosphate backbone between U52 and C53 that shifted away from A48 to avoid sterical clash (**Figure S7**). Subsequently, in the early stages of the simulations, namely during thermal equilibration, such reconfiguration of U52-C53 sugar-phosphate backbone resulted in destabilization of the U52(H3)...A48(O2') hydrogen bond and exposure of the U52 into solvent (**Figure S7**). All these rapid structural changes should not be considered as native structural dynamics of the riboswitch and are unambiguously a consequence of starting structure bias, namely non-native refinement of A48 *anti* orientation. Thus, in agreement with the observed electron density, we found that *anti*-oriented A48 is not compatible with the overall structure of Conformer 2 containing open-conformation of loop L3. Thus, crystallographic data together with MD simulations provide clear evidence of *syn*-orientated A48 in this particular L3 loop conformation; the MD simulations of Conformer 2 started with *anti*-A48 were not further analyzed and discussed.

For the sake of completeness, it is worth noting that MD simulations of Conformer 1 (containing closed conformation of loop L3 and A48 clearly resolved as *anti*-orientated) did not reveal any rapid structural changes during the early stage relaxation that would point to any doubts of the refinement of the L3 loop conformation.

**Figure S6**

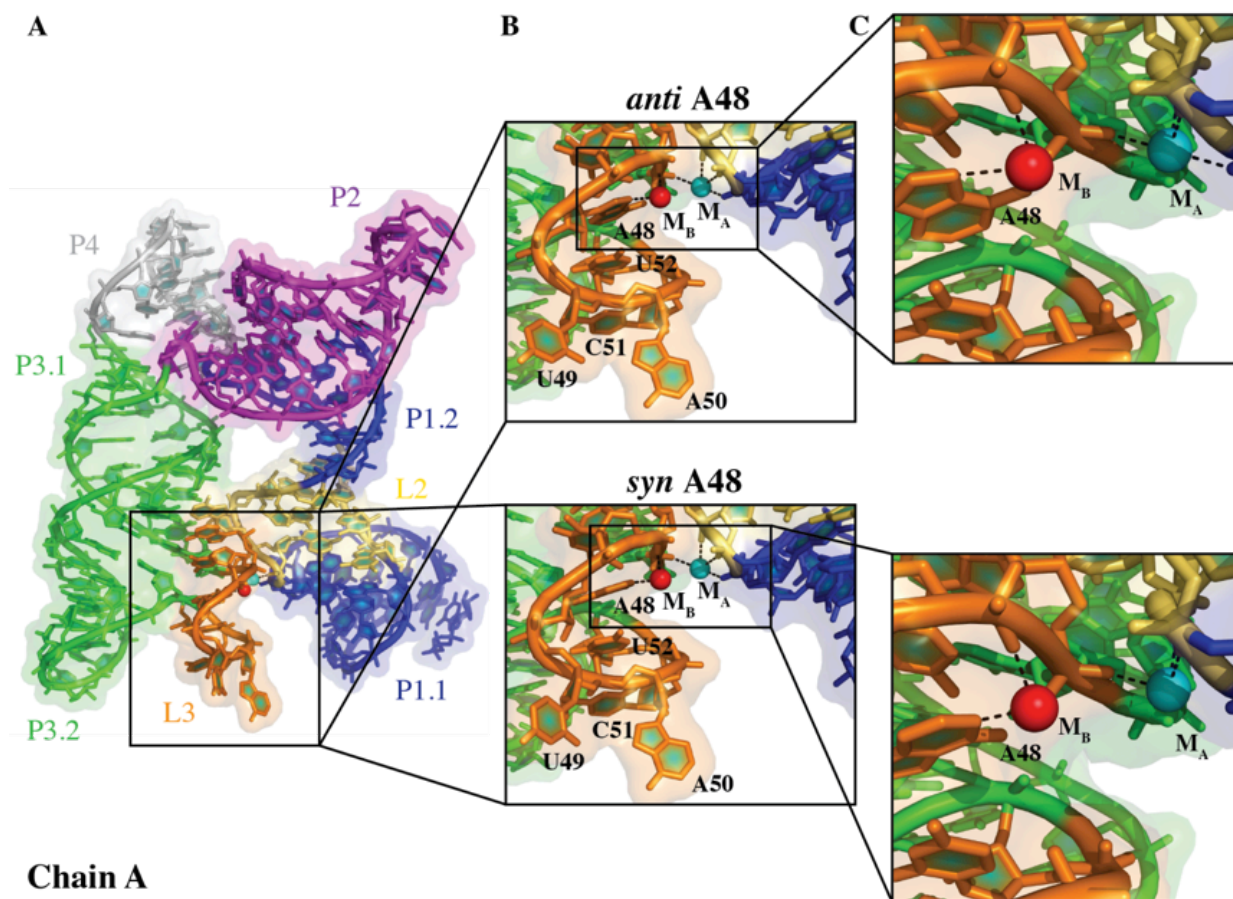


**Figure S6** Structure of *X. oryzae* aptamer domain of conformer 2 showing alternative *syn* and *anti* orientations of A48.

**Figure S7**

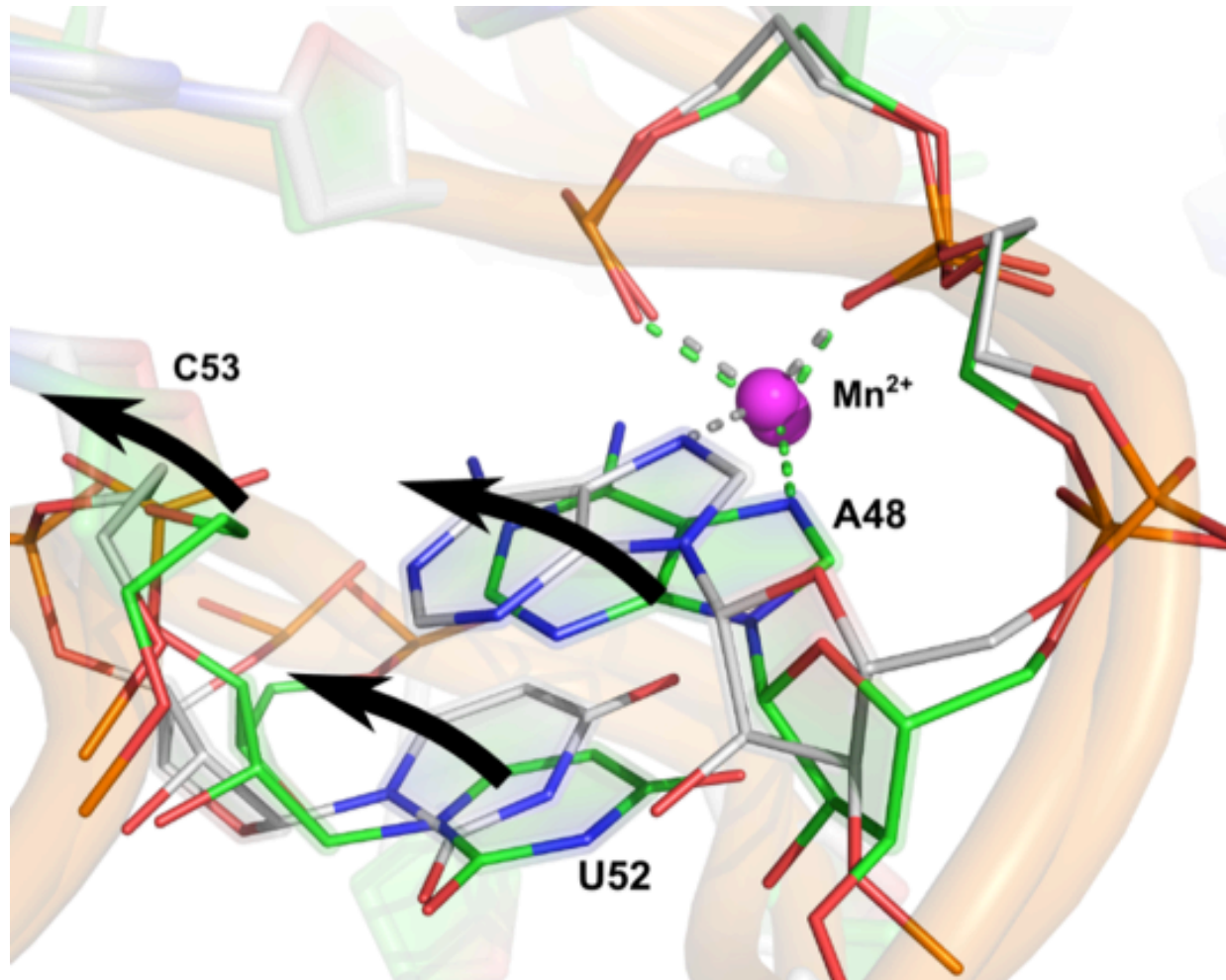


**Figure S7|** Structural changes observed during early stages of the MD simulations of *X. oryzae* conformer 2 with *anti*-orientation of A48. Green structure corresponds to crystal structure, while the silver refers to the structure after initial rearrangements during these early stages.

**Table S2** - Percentage of native stacking preserved in L3 loop during MD simulations (based on annotations calculated by baRNaba software) and percentage of occupancy of ions in the ion binding sites.

Ions		Stacking interactions [%]						Occupancy of M <sub>A</sub> [%]					Occupancy of M <sub>B</sub> [%]					
M <sub>A</sub>	M <sub>B</sub>	A9	U39	C40	A41	U44	A42	G7	G8	A9	U39	C45	G8	U39	C40	A41	U44	C45
		U39	C40	A41	C45	C45	U44	OP1	OP2	OP1	OP1	OP1	OP1	OP2	OP2	N7	OP1	OP2
<i>L.lactis</i>	Mg <sup>2+</sup>	Mn <sup>2+</sup>	100	98	77	98	92	76	100	100	100	100	100	100	100	100	100	100
	K <sup>+</sup>	Mn <sup>2+</sup>	99	99	78	96	65	83	100	100	100	100	2	100	100	100	100	100
	Mg <sup>2+</sup>	K <sup>+</sup>	99	99	2	4	5	6	100	100	100	100	100	100	100	98	6	0
	K <sup>+</sup>	K <sup>+</sup>	100	93	64	88	36	42	95	98	95	100	0	27	99	78	97	42
		A10	A46	C47	A48	C51	A50	G8	G9	A10	A46	U52	G9	A46	C47	A48	C51	U52
		A46	C47	A48	U52	U52	C51	OP2	OP2	OP1	OP1	OP1	OP1	OP2	OP2	N7/1	OP1	OP2
<i>X.ory</i> _cf2_syn	Mg <sup>2+</sup>	Mn <sup>2+</sup>	100	100	100	66	61	63	100	100	100	100	0	0	100	100	100	0
	K <sup>+</sup>	Mn <sup>2+</sup>	91	100	100	81	86	89	99	99	100	100	0	0	100	100	100	0
	Mg <sup>2+</sup>	K <sup>+</sup>	100	99	87	69	82	89	100	100	100	100	0	65	68	67	68	17
	K <sup>+</sup>	K <sup>+</sup>	96	99	89	70	90	67	95	98	98	98	45	6	90	67	68	10
<i>X.ory</i> _cf1_1	Mg <sup>2+</sup>	Mn <sup>2+</sup>	100	100	54	92	84	11	0	100	0	100	100	100	100	100	100	100
	K <sup>+</sup>	Mn <sup>2+</sup>	98	96	70	75	70	47	99	100	100	100	1	100	100	100	100	100
	Mg <sup>2+</sup>	K <sup>+</sup>	99	86	5	1	5	2	0	100	0	100	100	25	24	21	6	5
	K <sup>+</sup>	K <sup>+</sup>	97	99	76	69	78	86	79	85	79	92	11	20	85	74	82	19
<i>X.ory</i> _cf1_2	Mg <sup>2+</sup>	Mn <sup>2+</sup>	100	99	57	90	86	3	0	100	0	100	100	100	100	100	100	100
	K <sup>+</sup>	Mn <sup>2+</sup>	93	97	82	45	86	11	99	100	99	100	1	100	100	100	100	100
	Mg <sup>2+</sup>	K <sup>+</sup>	100	99	84	2	15	24	0	100	0	100	100	99	99	100	25	4
	K <sup>+</sup>	K <sup>+</sup>	87	95	54	37	47	60	35	94	62	97	5	72	34	83	76	59

**Figure S8**

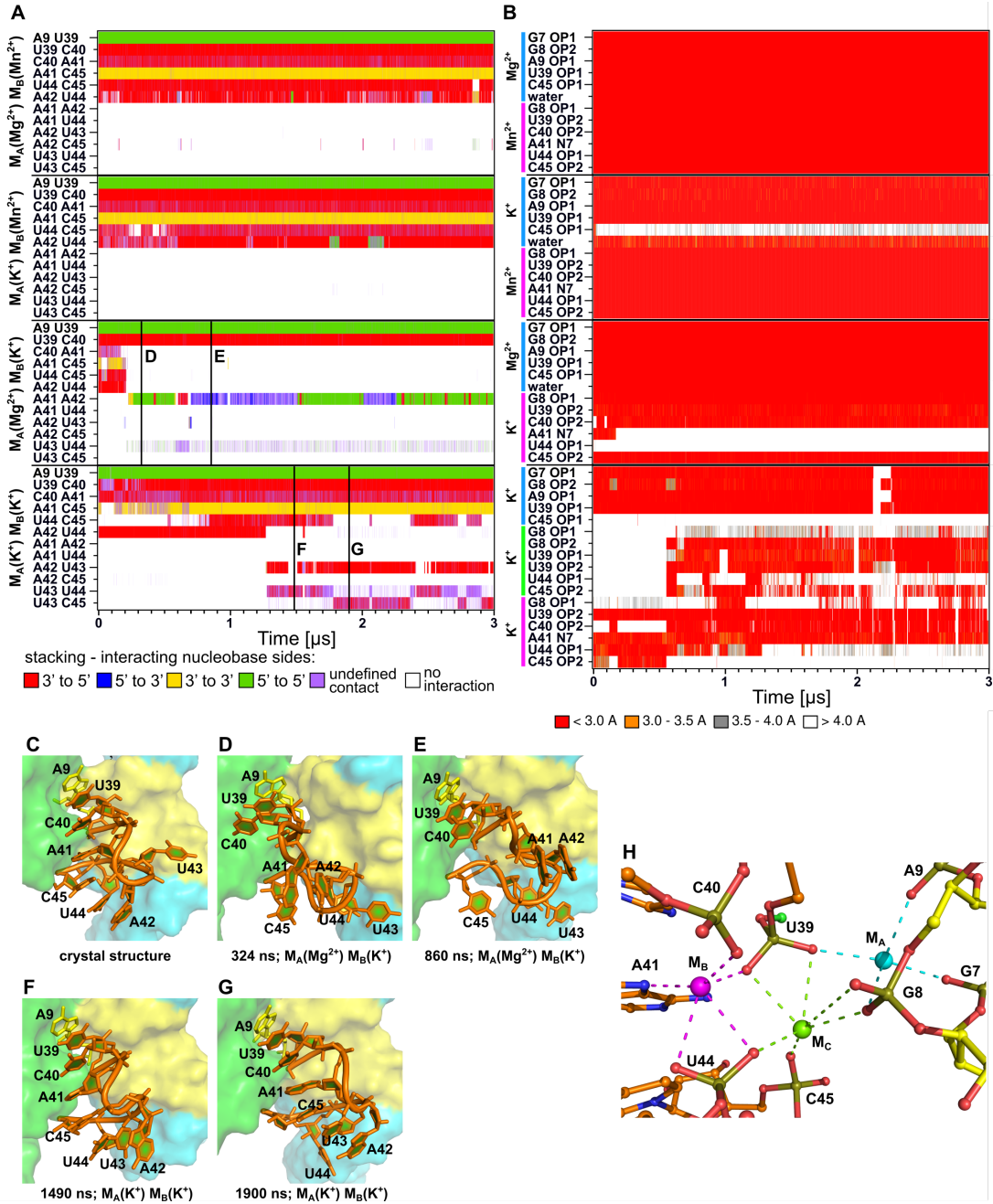


**Figure S8I** Conformational behavior of the L3 loop and  $M_A$  and  $M_B$  ion binding sites in MD simulation of *L. lactis* aptamer. A) Time evolution of the stacking pattern of the loop; the colors correspond to different mutual orientations of nucleobases in stacking interactions indicated by the corresponding faces (3'-face and 5'-face) exposed to the stacking interaction by stacked nucleobases. B) Time evolution of ligand-ion interactions in the ion binding sites. C-G) Close view on stacking pattern, panel C corresponds to crystal structure, while the others depict structures observed in MD simulations. H) New ion binding sites in simulation where both divalents were replaced by  $K^+$ .



# Conformer 1 simulation 1

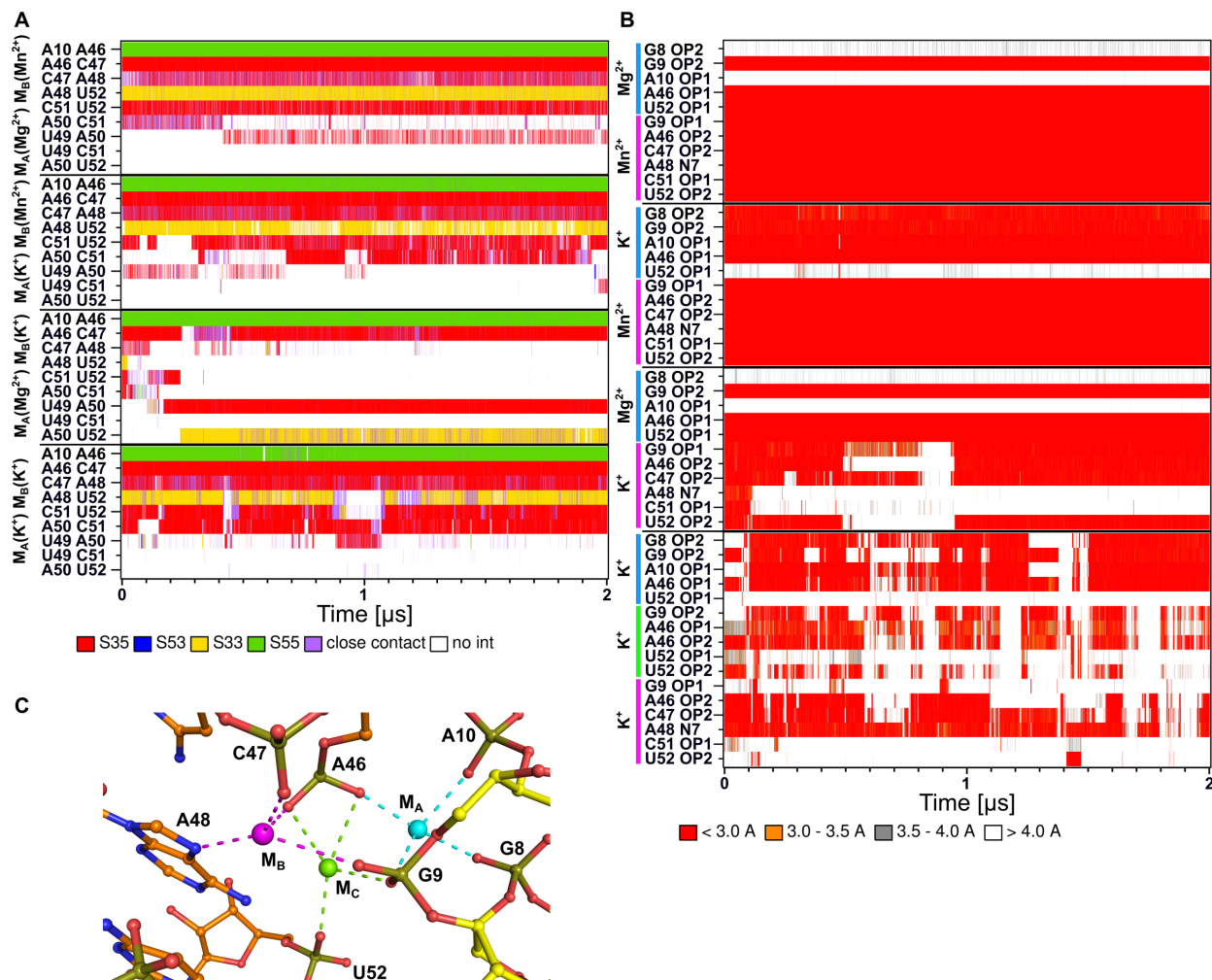


Figure S8. Continuation

# Conformer 1 simulation 2

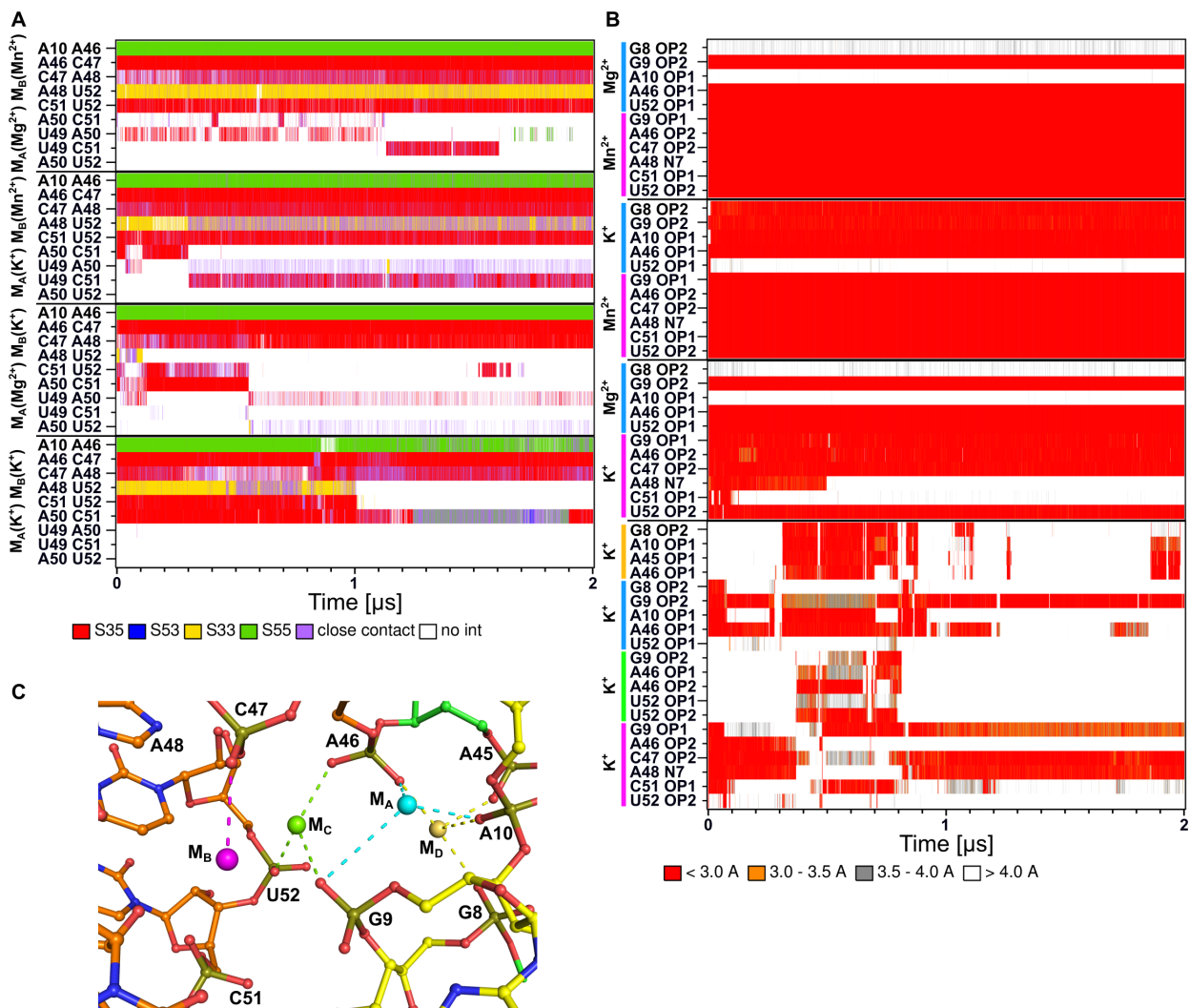
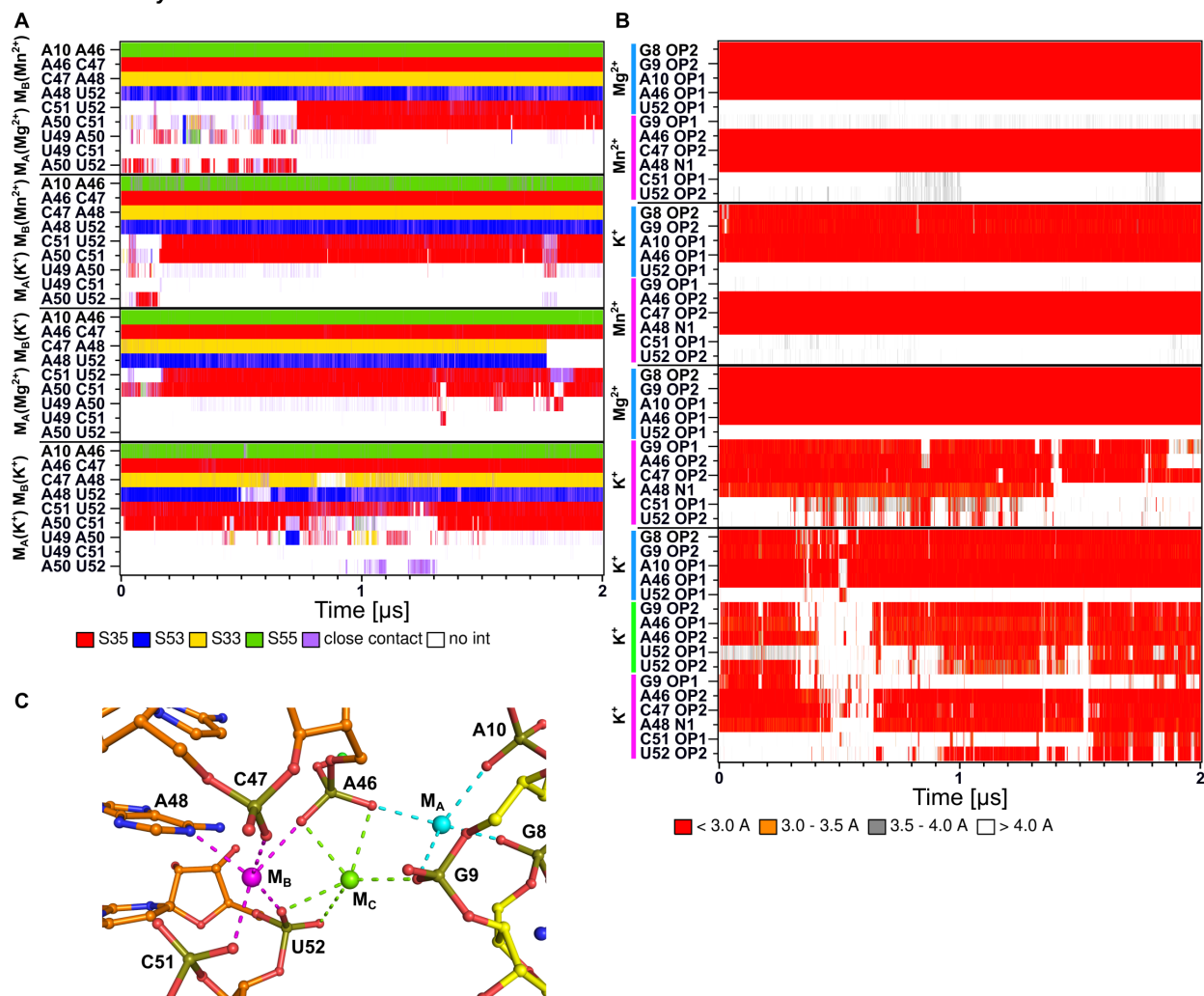


Figure S8. Continuation



# Figure S9

Conformer 2 syn A48



**Figure S9** Conformational behavior of the L3 loop and M<sub>A</sub> and M<sub>B</sub> ion binding sites in MD simulation of *X. oryzae* aptamer. **A)** Time evolution of the stacking pattern. **B)** Time evolution of ligand-ion interactions in the ion binding sites. **C)** New ion binding sites in simulation where both divalents were replaced by K<sup>+</sup>.

### Stacking pattern of L3

Most of the nucleobases from L3 loop form continuous stacking pattern (**Figure S4 D,E**, Figure S11). This segment is further stacked by its 5'-end on adenine A10 (A9 according to numbering of *L. lactis*) from L1 loop, which forms type I A-minor interaction with G66=C44 (G61=C37 according to numbering of *L. lactis*) base pair. This A-minor interaction together with part of the stacking pattern formed by the A10(A9) adenine and two nucleotides at 5'-end of L3 loop (i.e., A10|A46|C47 and A9|U39|C40 in simulation of structure from *X. oryzae* and *L. lactis*, respectively) represent rather rigid part of the stacking pattern, which was found to be stable in all ionic conditions (**Figures S8-S9** and **Table S2**). In addition to the A-minor interaction making tertiary contact between L1 and L3 loops, the above-mentioned A10|A46|C47 (A9|U39|C40) part of the stacking pattern is stabilized also by other tertiary interactions such as hydrogen bonding of C47 (C40 according to numbering of *L. lactis*) cytosine with riboses of C53 and A45 (G46 and G38 in *L. lactis*) of the P3.2 stem (see Figures S11 and S12 for evolution of all tertiary contacts between A10|A46|C47 (A9|U39|C40) part of the stacking pattern and its structural environment). The insensitivity of this region to types of ions in  $M_A$  and  $M_B$  sites suggests that the L1-L3 loop tertiary contact mediated by this pattern might be formed in all ionic conditions even if  $M_A$  and  $M_B$  sites are not yet properly formed and occupied by the corresponding divalent ions.

The rest of stacking pattern of L3 loop (i.e., A48|U52|C51|A50 and A41|C45|U44|U43 in *X. oryzae* and *L. lactis* structures, respectively) showed different dynamics depending mostly on the type of ion in  $M_B$  site (**Figures S8-S9** and **Table S2**). The presence of  $Mn^{2+}$  ion in  $M_B$  significantly stabilized native stacking pattern in L3 loop, while this pattern was destabilized in simulations where the  $Mn^{2+}$  ion was replaced by  $K^+$ . Surprisingly, when both divalent ions were replaced by  $K^+$  ions, the stability of L3 loop stacking pattern was higher than in case where only  $Mn^{2+}$  ion in  $M_B$  site was replaced by monovalent while  $M_A$  was occupied by  $Mg^{2+}$  ion, though still less stable than in simulations having also  $M_B$  site occupied by  $Mn^{2+}$ . In order to explain this observation, we hypothesize that stacking pattern of L3 loop represents inherently quite stable conformation of this loop capable of remaining stable on at least microsecond time scale. However, when  $M_A$  binding site is occupied by  $Mg^{2+}$ , unlike  $K^+$ , it enforces proper positioning of A46 and U52 (U39 and C45 according *L. lactis* numbering) phosphates which leads to destabilization of the stacking pattern of L3. This stacking-structure-destabilization effect of  $Mg^{2+}$  can be overcompensated only by binding of  $Mn^{2+}$  ion into the  $M_B$  binding site.

**Figure S10**

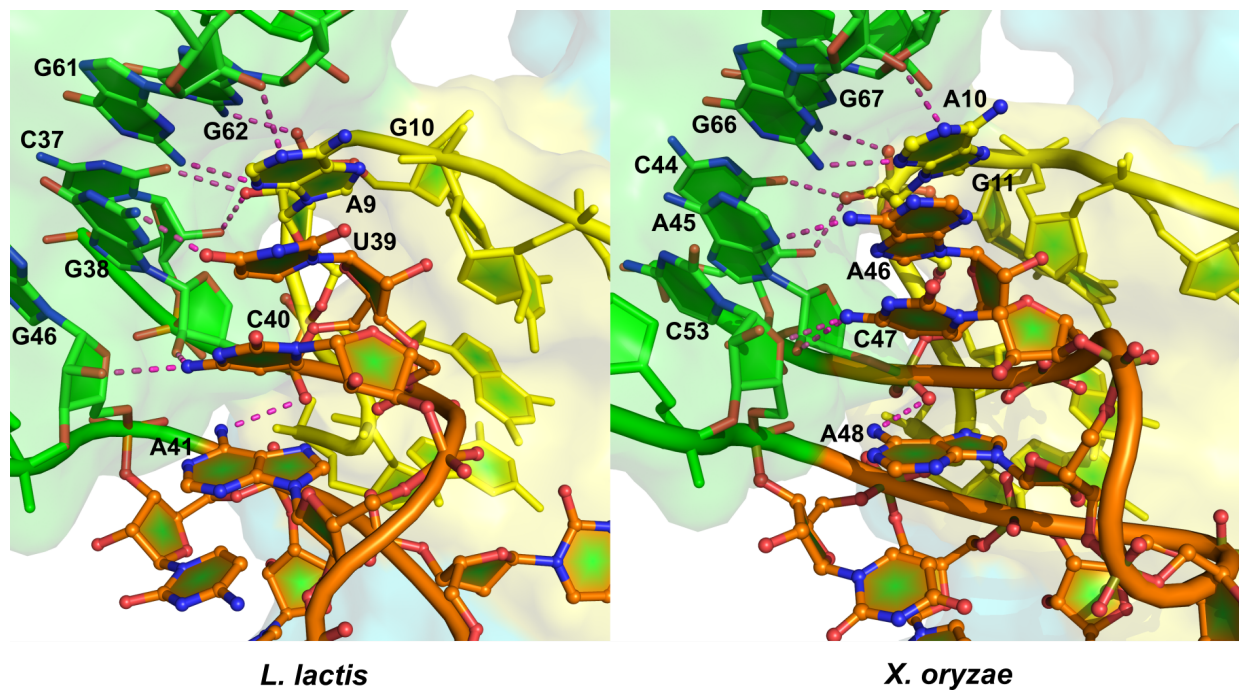


**Figure S10** The stacking pattern formed by A10 (A9 according to numbering of *L. lactis*) and nucleobases of loop L3 with depicted tertiary interactions (see **Figure S11** for their structural stabilities in MD simulations).

**Figure S11**

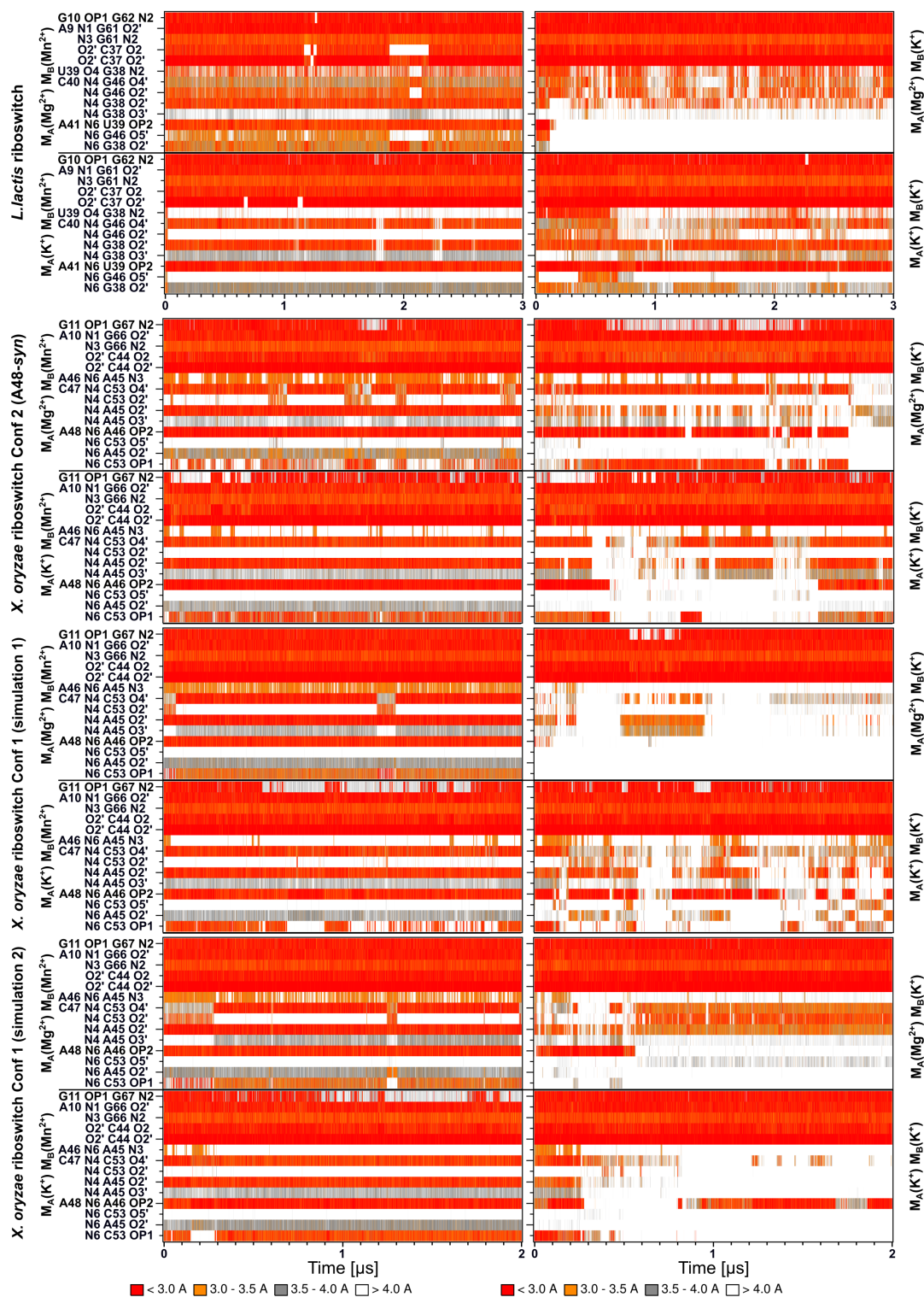


**Figure S11|** Time evolution of tertiary interactions of nucleotides included in the stacking pattern of L3 loop (see **Figure S10** for structural view of these tertiary contacts).

### ***Structural dynamics of SRL-like conformation of L1 in different structural contexts***

Besides structures of whole aptamer which all remained in docked state in our simulations, we also performed simulations of the structures consisting only of P1.1, P1.2 and L1 (based on *X. oryzae* – Conformers 1 and 2 and *L. lactis* crystal structures, see Table S2). Such minimalistic structure obviously lacks all tertiary contacts to L3 loop and P3 stem and thus its dynamics should correspond to the dynamics of this particular part in undocked state.

The base-pairing (**Figure S12**) as well as backbone conformation were monitored and compared to the corresponding values observed in the simulations of complete aptamer, i.e., in docked state. Note that the overall conformation of L1 loop as well as base pairing in P1.1 stem (with exception of terminal AU pairs of the P1.1 stem in simulation of *L. lactis* aptamer which revealed base pair fraying) were entirely stable in the simulations of complete aptamers. The most significant structural changes were observed in simulation of the isolated P1.2L1P1.1 structure based on Conformer 2 of the *X. oryzae* structure. The disruption of G9(N1)...G93(N7) H-bond was followed by reformation of G8-A94 from *t*SH into *c*WC base pairing and loss of the S-turn conformation of the sugar-phosphate backbone of G8-A10. Interestingly, the simulation of the same structural motif derived from the Conformer 1 of *X. oryzae* crystal structure showed less pronounced changes, in particular, the G9(N1)...G93(N7) H bond was broken and recreated several times. Finally, in case of the simulation based on *L. lactis* structure, the L1 loop resembled conformation observed in the complete aptamer; however, we observed rather significant unpairing in P1.1 stem. This may be due to a weaker P1.1 in *L. lactis* that is shorter by 1-bp and has three A-U base pairs capping the stem, as opposed to the two G-C base pairs in the *X. oryzae* structure.

In summary, the data indicate that when A10 is sequestered in the A-minor interaction, the P1.2L1P1.1 segment adopts a conformation resembling the topology of a canonical sarcin-ricin loop. Compared to the sarcin-ricin loop consensus sequence, the A10 nt is inserted between its GpU platform and the flexible region. In addition, the trans-Hoogsteen/Hoogsteen base pair in the flexible region adjacent to the GpU platform is replaced by a trans-Watson-Crick/Hoogsteen pair. When the A10 is not involved in the tertiary interaction, it instead destabilizes the SRL-like topology.

# Figure S12

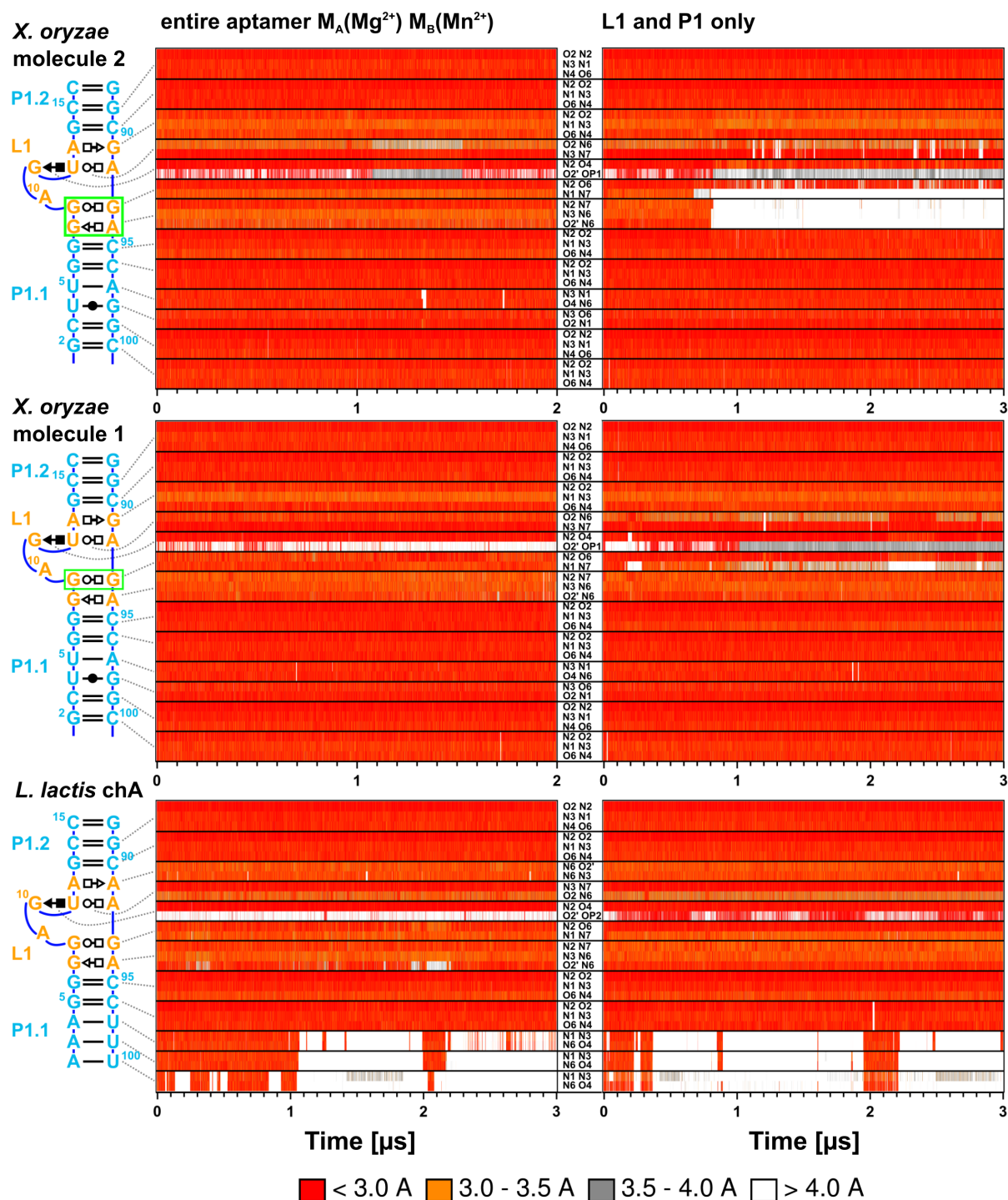
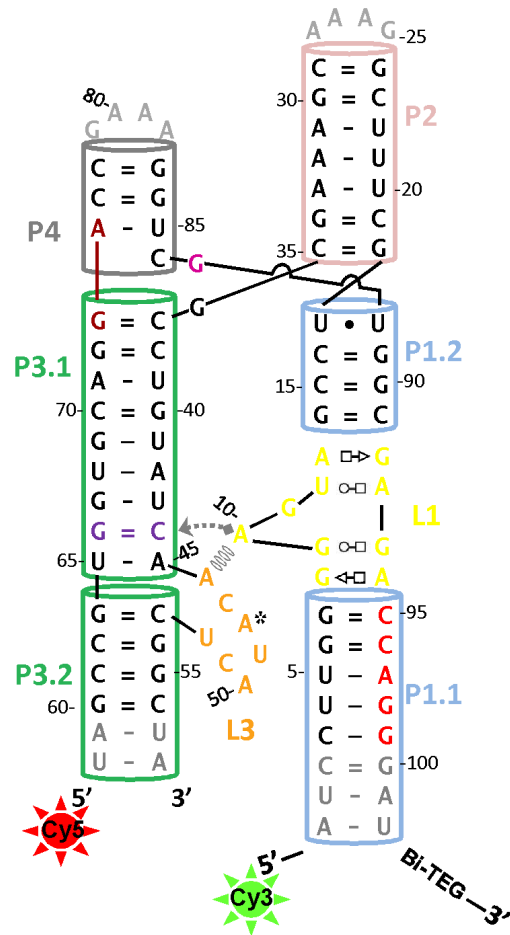


**Figure S12.** Time evolution of native base pairing interactions of SRL-like motif of L1 in entire aptamer and in model structure (consisting only of P1.1, P1.2 and L1 and thus lacking A-minor interaction of A10 in *X. oryzae* and A9 in *L. lactis*, to L3 loop and P3 stem). The most labile interactions are highlighted in green.

**Figure S13**

**a**



**b**

**Oligo 1**

5' -**Cy3**-AUCCUUGGGAGUAGCCUGCUUUCUUCGAAAGCGCCUGUAUCAACAUACUCGGCUA-3'

**Oligo 2**

5' -**Cy5**-UAGCCGUGGUGCAGGCAACGGCGAAAGCCGUCUGG**AGAGACCAGGGAU**-BioTEG-3'

**Figure S13** | smFRET construct design. **(a)** Sequence and secondary structure of the *Xory yybP-ykoY* riboswitch construct used for smFRET. The construct was made by hybridizing two chemically synthesized RNA oligonucleotides modified at their 5' and 3' ends with Cy3, Cy5 fluorophores and Biotin-TEG. **(b)** Sequences of the two oligonucleotides with modifications used for the smFRET construct shown in (a)



**Figure S14**

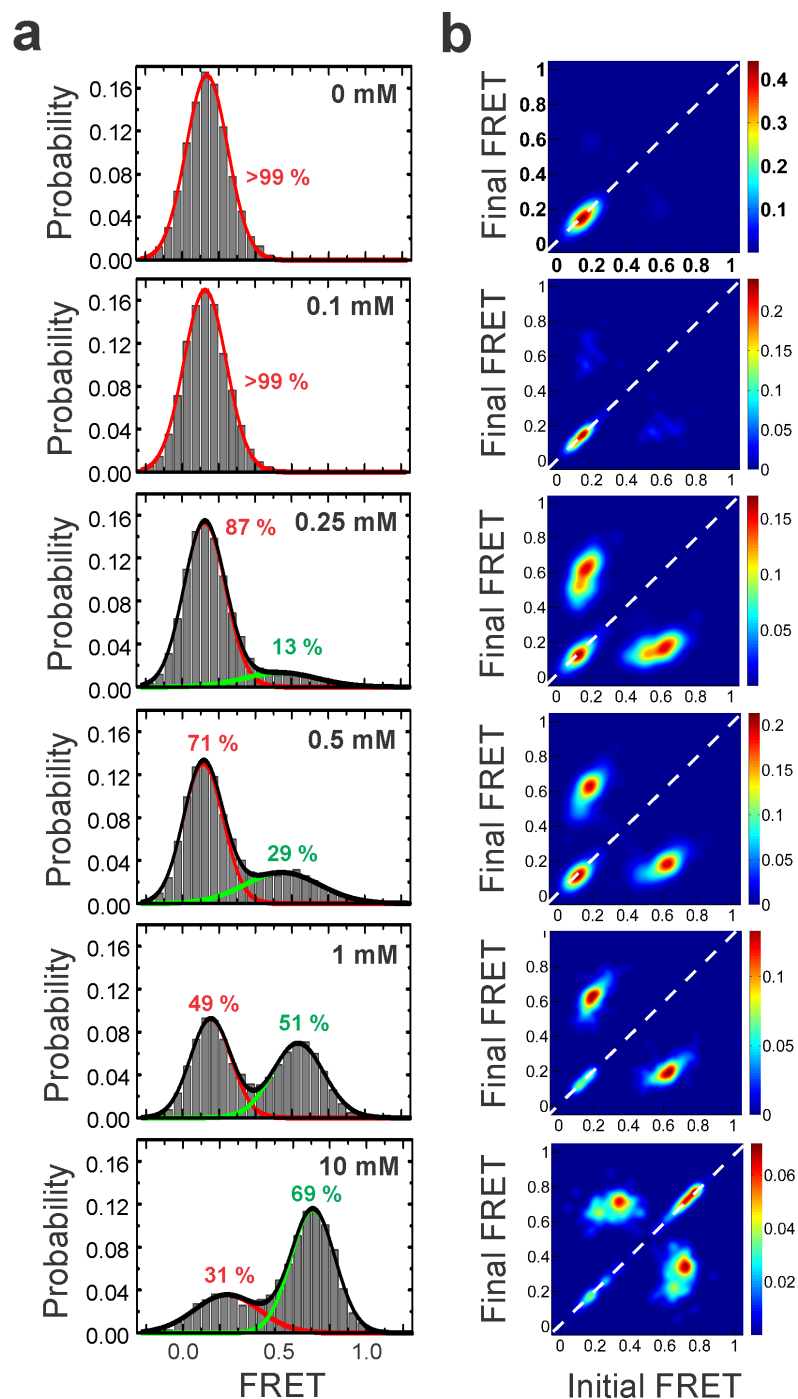


**Figure S14|  $\text{Mg}^{2+}$  titration of the WT *Xory* riboswitch.** (a) FRET histograms showing the distribution of the two FRET states under various  $\text{Mg}^{2+}$  concentrations, fit to a sum of Gaussian functions. The Gaussian peaks for the low- and high-FRET states are shown in red and green, respectively, while the cumulative fit is shown in black. The histograms under 0 mM and 0.1 mM contain very low populations of the high-FRET state and were fit to a single Gaussian function. (b) TODPs under different  $\text{Mg}^{2+}$  concentrations showing the fraction of static 'on-diagonal' and dynamic 'off-diagonal' molecules. The SD populations under the high, 10 mM  $\text{Mg}^{2+}$  is evident in the TODP.



**Figure S15**

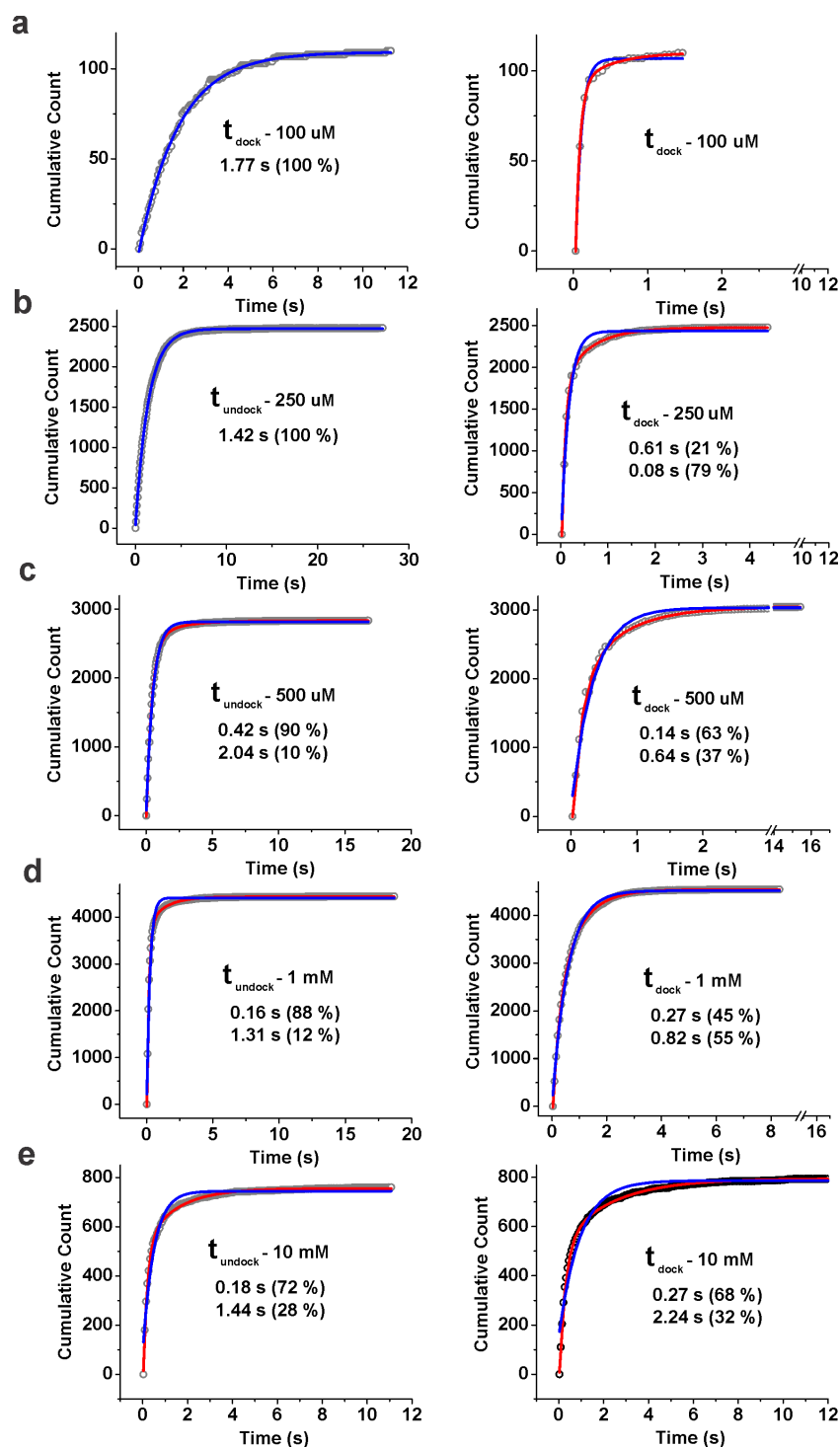


**Figure S15| Kinetics of WT *Xory*  $\text{Mn}^{2+}$  sensing riboswitch.** (a) Cumulative dwell-time distributions of  $t_{\text{undock}}$  and  $t_{\text{dock}}$  in the presence of 0.1 mM  $\text{MgCl}_2$  fit to single (blue) and double-exponential (red) are shown. The life-times and amplitudes of slow and fast components are also shown. In case of double-exponential fits, fit to single exponential function is also shown for comparison. (b-e) Same as in (a) but in the presence of 0.25 mM, 0.5 mM, 1 mM and 10 mM  $\text{MgCl}_2$ , respectively.

**Figure S16**

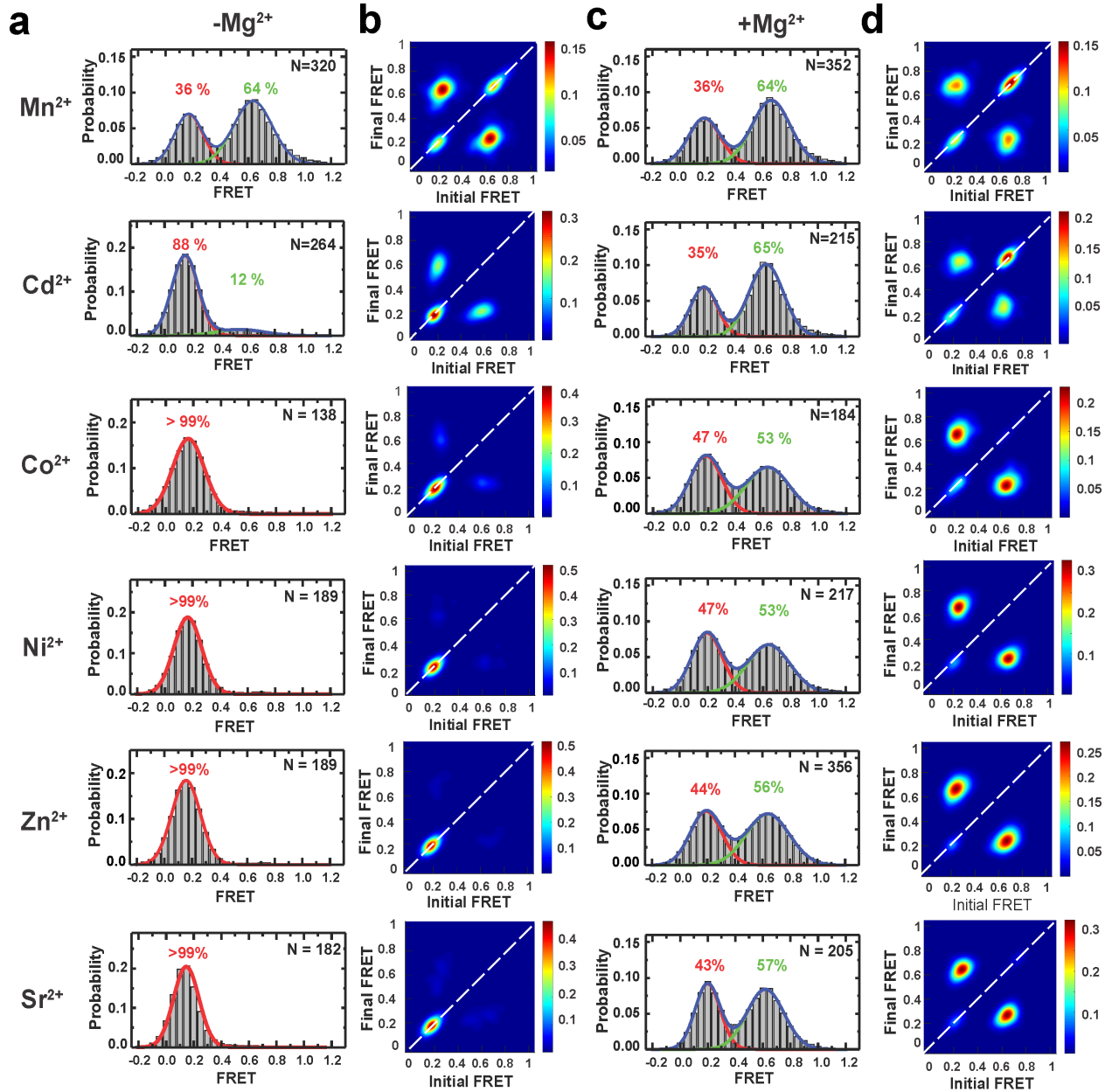


**Figure S16| Effect of different metal ions on the WT *Xory* riboswitch. (a)** FRET histograms showing equilibrium distribution of docked and undocked conformations of the WT riboswitch at 0.1 mM concentration of different transition metal ions alone (i.e., in the absence of 1 mM  $MgCl_2$ ). Gaussian fits to the docked, undocked are shown as green and red curves, while the cumulative fit is shown in blue. The number of molecules, N, for each condition analyzed and the % of docked and undocked conformations in each condition are indicated. **(b)** TODPs corresponding to the histograms in (a). **(c)** FRET histograms and **(d)** TODPs at 0.1 mM concentration of different metal ions in the presence of 1 mM  $MgCl_2$ . For the different metal ions tested, except  $Mn^{2+}$  and  $Cd^{2+}$ , almost all the traces remained in SU conformation, with >95 % in the low-FRET ( $\sim 0.1$ ) undocked conformation, in the absence of  $Mg^{2+}$ .

### **The *yybP-ykoY* riboswitch can discriminate between similar transition metal ions**

The selectivity of the *Xory* riboswitch for  $\text{Mn}^{2+}$  over  $\text{Mg}^{2+}$  arises in part from the inner-sphere contact with A48(N7), suggesting that other soft transition metal ions may also be recognized<sup>1</sup>. To test this hypothesis, we probed the effects of different divalent metal ions on the conformation of the riboswitch, at 0.1 mM concentration alone or in the presence of 1 mM  $\text{Mg}^{2+}$ . FRET histograms showed that out of all the different metal ions tested,  $\text{Cd}^{2+}$  is most effective in promoting docked conformations (**Fig. 5b, Supplementary Fig. 16**). In the presence of 1 mM  $\text{Mg}^{2+}$ , addition of 0.1 mM  $\text{Cd}^{2+}$  resulted in ~65 % of the high-FRET docked conformation, comparable to the docked population upon addition of 0.1 mM  $\text{Mn}^{2+}$ . Examination of individual smFRET traces as well as the TODP showed that this is due to a large fraction of SD traces (**Supplementary Fig. 16**), in agreement with the tight binding of  $\text{Cd}^{2+}$  to the *yybP-ykoY* riboswitch shown recently<sup>1</sup>. Among the other metals tested,  $\text{Ni}^{2+}$ ,  $\text{Co}^{2+}$ ,  $\text{Sr}^{2+}$  or  $\text{Zn}^{2+}$  had little effect on promoting the folded conformations of the riboswitch under these conditions. Interestingly, in the absence of  $\text{Mg}^{2+}$ , while 0.1 mM  $\text{Mn}^{2+}$  alone led to the appearance of DD and SD traces with ~62 % docked population (mean FRET  $0.67 \pm 0.12$ ) (**Fig. 5c**), 0.1 mM of  $\text{Ni}^{2+}$ ,  $\text{Co}^{2+}$ ,  $\text{Sr}^{2+}$  or  $\text{Zn}^{2+}$  did not affect SU traces and  $\text{Cd}^{2+}$  had only a small effect in promoting DD traces (**Supplementary Fig. 16**). This suggests that, while  $\text{Mg}^{2+}$  and  $\text{Mn}^{2+}$  may both bind at  $M_{A,Mg}$ ,  $\text{Cd}^{2+}$  may be more specific to the  $M_{B,Mn}$  site. These results suggest that while the *Xory* riboswitch has some degree of plasticity in recognizing ligands, in a background of  $\text{Mg}^{2+}$  it preferentially recognizes  $\text{Mn}^{2+}$  and  $\text{Cd}^{2+}$  and can effectively discriminate against similar divalent transition metal ions.

**Figure S17**

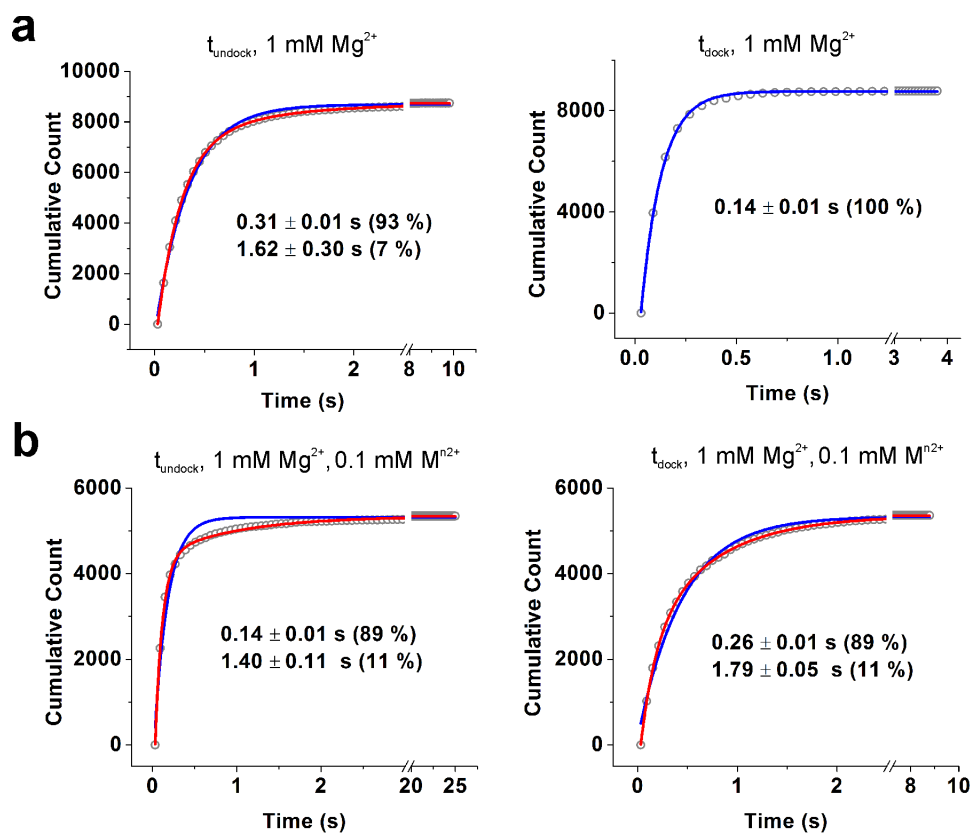


**Figure S17| Kinetics of the *Xory* riboswitch A48U mutant.** (a) Cumulative dwell-time distributions of  $t_{\text{undock}}$  and  $t_{\text{dock}}$  in the presence of  $1 \text{ mM MgCl}_2$  fit with single (blue) and double-exponential (red) functions. The life-times and amplitudes of slow and fast components are also shown. In the case of double-exponential fits, fit to single exponential is also shown for comparison. (b) Same as in (a) but in the presence of  $1 \text{ mM MgCl}_2$  and  $0.1 \text{ mM MnCl}_2$ .

## Supplementary References

1. Bachas, S.T. & Ferre-D'Amare, A.R. Convergent Use of Heptacoordination for Cation Selectivity by RNA and Protein Metalloregulators. *Cell Chem Biol* **25**, 962-973 e965 (2018).
2. Begg, S.L. *et al.* Dysregulation of transition metal ion homeostasis is the molecular basis for cadmium toxicity in *Streptococcus pneumoniae*. *Nat Commun* **6**, 6418 (2015).
3. Kuhrova, P., Banas, P., Best, R.B., Sponer, J. & Otyepka, M. Computer Folding of RNA Tetraloops? Are We There Yet? *J Chem Theory Comput* **9**, 2115-2125 (2013).
4. Sponer, J.E. *et al.* Theoretical studies on the intermolecular interactions of potentially primordial base-pair analogues. *Chemistry* **16**, 3057-3065 (2010).
5. Menger, M., Eckstein, F. & Porschke, D. Dynamics of the RNA hairpin GNRA tetraloop. *Biochemistry* **39**, 4500-4507 (2000).
6. Zhao, L. & Xia, T. Direct revelation of multiple conformations in RNA by femtosecond dynamics. *J Am Chem Soc* **129**, 4118-4119 (2007).
7. Kuhrova, P. *et al.* Computer Folding of RNA Tetraloops: Identification of Key Force Field Deficiencies. *J Chem Theory Comput* **12**, 4534-4548 (2016).